International Journal of Mechanical Sciences 333 (2027) 112274

Contents lists available at ScienceDirect

International Journal of Mechanical Sciences

journal homepage: www.elsevier.com/locate/ijmecsci

Strain-stiffening effects on electro-mechanical wrinkling of soft dielectric film–substrate systems☆,☆☆

Linghao Kong [a], Liang Si [a], Renwei Mao [c], Michel Destrade [a,b,*], Bin Wu [a,*]

[a] Key Laboratory of Soft Machines and Smart Devices of Zhejiang Province, Department of Engineering Mechanics, and Soft Matter Research Center, Zhejiang University, Hangzhou, 310027, PR China
[b] School of Mathematical and Statistical Sciences, University of Galway, University Road, Galway, Ireland
[c] Intelligent Structures and Advanced Equipments Technology Center, Huanjiang Laboratory, Zhuji, 311816, PR China

ARTICLE INFO

Keywords:
Wrinkling instability
Strain stiffening
Dielectric elastomer
Film–substrate system
Stroh formulation
Post-buckling analysis
Multiphysics finite element simulations

ABSTRACT

Strain-stiffening is a common feature in soft dielectric elastomers, but its effects on the electro-mechanical wrinkling of film–substrate systems remain insufficiently understood. Here we derive exact analytical solutions for this wrinkling bifurcation by adopting the Gent model to characterize strain stiffening. Critical Gent parameters are determined to partition the parameter space into multiple wrinkling regimes governed by the prescribed stretch λ and shear-modulus ratio. We show that ignoring the strain-stiffening effect can lead to incorrect stability evaluations and considerable errors in the critical voltage, with significant deviations occurring under large tensile pre-stretch or strong pre-compression. Moreover, the effect of strain stiffening depends on its distribution between the two layers: when both layers have identical Gent parameters, stronger strain stiffening increases the critical voltage, whereas when it is present in the film alone, it decreases the critical voltage. Finally, full nonlinear finite element simulations validate our formulas and also provide post-buckling analyses. Results show a smooth, supercritical-like post-buckling response under weak-to-moderate pre-compression, with the wrinkle amplitude increasing continuously and stably beyond the critical voltage. On the other hand, strong pre-compression yields an abrupt amplitude increase at the critical voltage, a mechanism that requires further study. Accounting for strain stiffening is vital for safe design, and our work provides advances in electric-field-controlled morphologies for diverse soft functional devices.

1. Introduction

Soft dielectric materials, such as dielectric elastomers, represent a highly promising category of smart materials capable of reacting to external electric field stimulation [1–3], offering the advantages of significant deformability [4], giant actuation strains [5], low elastic modulus [6], and fast response [7]. Due to these exceptional electro-mechanical coupling properties, numerous potential applications have been put forward for dielectric materials, including artificial muscles [8–10], sensors [11,12], tunable lenses [13,14], electrical energy storage devices [15,16], energy transducers [17,18], soft robots [19,20], tunable resonators and waveguides [21–23], as well as tunable phononic crystals and metamaterials [24–27].

Surface wrinkling is a typical instability behavior commonly observed in soft materials, biological tissues, and engineered surfaces [28–31]. A most common configuration exhibiting this behavior is that of a perfectly bonded bilayer structure with a stiff film attached to a compliant substrate [3,32–35]. Natural examples of wrinkling patterns can be found in esophageal mucosa [36], cerebral folds [37,38], and human skin [39]. From an engineering perspective, controllable wrinkling has found diverse applications such as generating surface patterns, tuning optical performances [40], characterizing material surface features [41], designing non-lithographic phase masks [42], reducing effective surface tension [43], and developing high-performance flexible sensors [12,44].

☆ This article is part of a Special issue entitled: 'in honour of Prof Marian Wiercigrochs Birthday' published in International Journal of Mechanical Sciences.

☆☆ This work was supported by the National Natural Science Foundation of China (Nos. 12402107 and U24A2005), and the Baima Lake Laboratory Joint Fund of Zhejiang Provincial Natural Science Foundation of China (No. LBMHZ26E060007). Partial support was also provided by the High-Level University Discipline Innovation and Talent Introduction Project of China (No. B21034). The work of MD was supported by a Qiushi Guest Professor appointment (Seagull Program) at Zhejiang University.

* Corresponding authors.
E-mail addresses: linghaokong@zju.edu.cn (L. Kong), silianggltty@gmail.com (L. Si), rwmao@zju.edu.cn (R. Mao), michel.destrade@universityofgalway.ie (M. Destrade), bin.wu@zju.edu.cn (B. Wu).

https://doi.org/10.1016/j.ijmecsci.2026.112274
Received 31 July 2026; Received in revised form 10 October 2026; Accepted 6 November 2026
Available online 16 November 2026
0020-7403/© 2026 Elsevier Ltd. All rights are reserved, including those for text and data mining, AI training, and similar technologies.

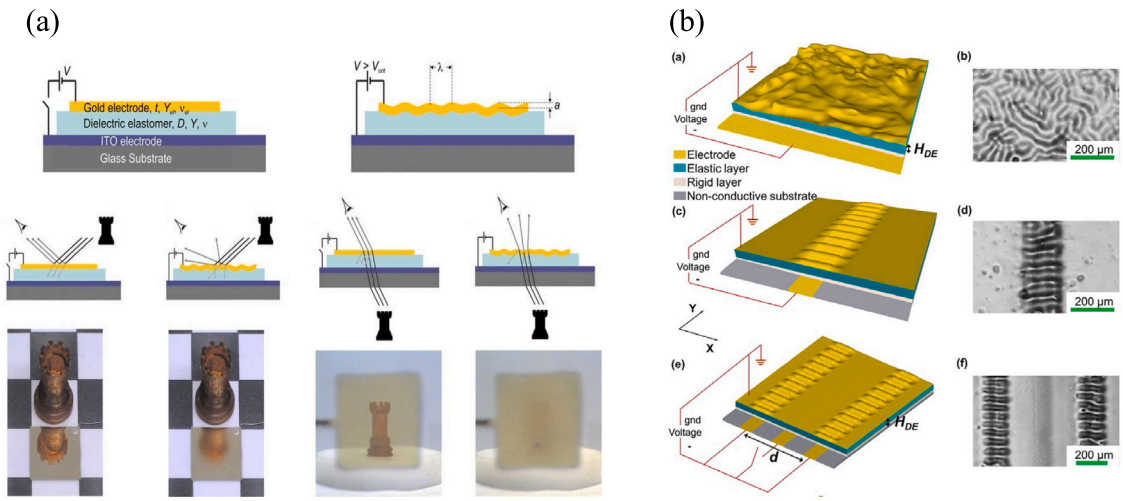


Fig. 1. Examples of electrically induced surface instabilities in dielectric film–substrate systems: (a) Voltage-actuated reversible wrinkling for binary optical switching between specular and diffuse reflection/transmission [52]; (b) Adjusting the spacing d between the underlying electrodes allows for the transition of wrinkle patterns from regular to random configurations [53].

Wrinkling is a classic research topic in mechanics, with extensive studies focusing on its formation mechanism and practical implementation. Specifically, Genzer and Groenewold [45] reviewed the formation and applications of surface wrinkles, while Audoly and Boudaoud [46] developed a theoretical model for the buckling of a stiff film bonded to a compliant substrate. Alawiye et al. [47] revisited the linear stability of elastic bilayers, and Martins et al. [48] proposed a modal theory for stretched membranes. More recent studies have examined post-buckling energy-barrier mechanisms, composite-electrode wrinkling, and the effects of pre-stretched substrate trilayers [49–51]. However, the coupling between Maxwell's field equations and continuum mechanics poses major difficulties for exploring instabilities in dielectric film–substrate structures [3]. On the other hand, the reversibility of the electro-mechanical coupling makes electric-field-triggered wrinkling ideal for programmable surface morphing. Accordingly, precise electric-field modulation of wrinkle morphology is a prerequisite for advancing functional applications. For example, Van den Ende et al. [52] achieved reversible wrinkling on elastomeric coatings via voltage actuation. Their system realizes binary optical switching between specular and diffuse reflection/transmission, demonstrating the feasibility of electric-field-induced wrinkling (see Fig. 1(a)). Lin et al. [53] realized tunable electric-field-induced wrinkling on film–substrate structures by adjusting the spacing between underlying electrodes, as illustrated in Fig. 1(b). The wrinkle patterns can switch between ordered and random states, enabling multifunctional optical devices integrating reflection, diffusion, and diffraction gratings. These patterns are formed not on a soft substrate as studied in this work, but on a rigid one, which limits the system's deformability but still illustrates key principles of electro-responsive wrinkling. Meanwhile, with the advent of low-voltage-driven (200 V) soft dielectric materials, more favorable conditions are now available for practical applications of soft dielectric materials in engineering [54].

To support rational design and performance optimization, it is crucial to elucidate the intrinsic instability behaviors of soft dielectric film–substrate systems. Studies of purely elastic film–substrate systems addressed linear instability and imperfection sensitivity [55–57]. Subsequent studies developed exact and semi-analytical descriptions of finite-wavelength wrinkling [58–61], while other works investigated post-buckling evolution, wrinkle-pattern selection, and finite-element modeling [62–64]. For dielectric film–substrate systems, Su et al. [65] studied voltage-driven bending of dielectric elastomer bilayers and realized accurate angle regulation via applied voltage, achieving programmable smart bending actuation. Sriram et al. [66] adopted a data-driven method to predict the initiation of wrinkling in composite dielectric bilayers under combined electro-mechanical loads. Wu et al. [3] investigated electro-mechanical wrinkling instabilities in soft dielectric film–substrate systems using neo-Hookean constitutive models. The critical thresholds for instability were derived analytically and validated by finite element simulations, thereby providing theoretical support for electric-field-regulated surface patterning in flexible functional devices.

Most existing theoretical models adopt linear elasticity or neo-Hookean hyperelasticity and ignore strain stiffening. However, in practical scenarios, large tensile pre-stretch and strong pre-compression can produce substantial deformation, making strain-stiffening effects significant [67]. To address this issue, the Gent model has been widely adopted to analyze electro-mechanical instabilities of standalone dielectric films. Related studies have confirmed its capability to capture stiffening characteristics. For example, Su et al. [68] studied electro-mechanical wrinkling of dielectric plates using the Gent model. They found that strain stiffening changes critical instability conditions and restricts the occurrence of large snap-through actuation. Dorfmann and Ogden [69] employed the Gent model to investigate electro-mechanical wrinkling and bifurcation of soft dielectrics, and revealed its distinct stability characteristics compared with neo-Hookean materials. Using the Gent type of strain energy density function, Gangwar et al. [70] revealed that strain stiffening and stretch-dependent permittivity significantly affect the stable taut domains and critical instability thresholds of dielectric elastomer membranes.

The studies reviewed above address complementary aspects of electro-mechanical instability. Wu et al. [3] developed a wrinkling analysis for a dielectric film bonded to a hyperelastic substrate using neo-Hookean constitutive models. The Gent-based studies discussed above [68–70] examined strain-stiffening effects primarily in standalone dielectric plates or membranes. However, the instabilities and pattern formation of dielectric films bonded to a hyperelastic substrate, with strain stiffening incorporated in either or both layers, have yet to be systematically analyzed theoretically and numerically. In particular, how finite-chain extensibility in the soft dielectric film and substrate modifies their coupled wrinkling response, especially when the two constituents have different Gent parameters, remains unresolved.

The present study addresses this question by incorporating Gent strain stiffening in either or both constituents of the soft dielectric film–substrate system shown in Fig. 2. Both constituents are assumed to be strictly incompressible and perfectly bonded, and the geometry consists of a finite-thickness dielectric film bonded to a semi-infinite

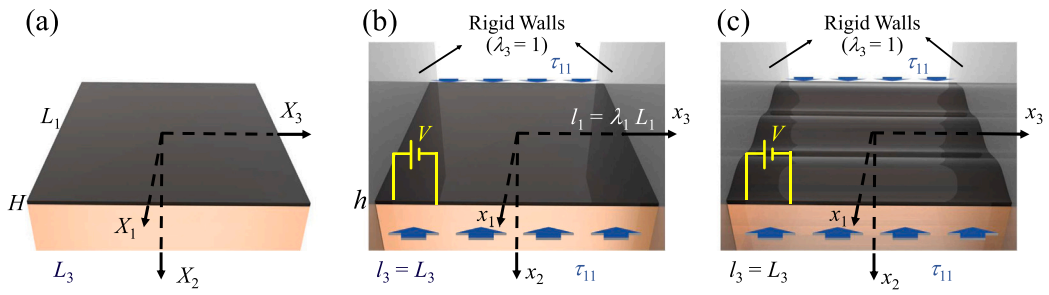


Fig. 2. Illustration of a soft dielectric film–substrate system subjected to plane-strain loading. (a) Initial undeformed configuration; (b) Current deformed configuration under the prescribed stretch λ_1 and applied voltage V, with plane-strain conditions ($\lambda_3 = 1$); (c) Surface wrinkling instability. The lateral traction arrows along the x_1 direction represent the reaction tractions required to maintain the prescribed stretch λ_1.

hyperelastic substrate under plane-strain deformation ($\lambda_3 = 1$). The film follows an ideal dielectric model with deformation-independent permittivity [3]. We focus on the practical scenario where the pre-stretch λ_1 is held fixed and the voltage V is increased, with the goal of triggering wrinkling at the minimal voltage.

Our objectives are to quantify how the Gent parameters, prescribed stretch, and initial shear-modulus ratio affect the critical voltage and critical wavelength; identify the zero-critical-voltage boundaries separating purely mechanical from voltage-induced wrinkling; and determine how these effects depend on whether strain stiffening acts in both layers or in the soft dielectric film alone. For this purpose, working within the framework of nonlinear electro-elasticity and its associated linearized incremental theory [71], we adopt the Stroh formulation and surface-impedance matrix method [3,68] to derive exact bifurcation equations for the soft dielectric film–substrate system by incorporating the strain-stiffening effect from the Gent constitutive model. Our analytical results reveal that neglecting the strain-stiffening effect characterized by the Gent model can cause severe under- or over-estimation of the critical voltage. This inevitably misjudges the onset of wrinkling instability and renders mechanical predictions and structural designs unreliable for dielectric film–substrate systems. These predictions are validated and extended by finite element simulations (COMSOL Multiphysics®), which confirm the critical voltage estimates and capture the post-buckling evolution of wrinkle patterns. The contribution lies in determining how the distribution of strain stiffening between the two layers modifies instability thresholds, regime boundaries, and post-buckling responses within this framework.

The remainder of this paper is organized as follows: Section 2 establishes the analytical model and derives exact solutions for the wrinkling instability along with detailed methodologies for finite element post-buckling analysis. A comprehensive analysis of the results is presented in Section 3, which systematically quantifies the influence of strain stiffening on wrinkling instability, alongside finite element verification and post-buckling analysis. Finally, Section 4 summarizes the principal findings and main contributions of this study.

2. Analytical and numerical modeling

2.1. Finite homogeneous deformation

The system consists of a soft semi-infinite elastic substrate and an elastic dielectric film bonded on its surface. In the initial undeformed configuration, the substrate and the film occupy the $X_2 > 0$ and $-H < X_2 < 0$ regions, respectively (see Fig. 2(a)), where (X_1, X_2, X_3) denote the Cartesian coordinates, H is the film thickness, and L_i $(i = 1, 3)$ denotes the lateral length in the X_i direction. In the current deformed configuration (see Fig. 2(b)), the film–substrate system undergoes a homogeneous deformation along the principal directions x_i (parallel to X_i), characterized by the principal stretches λ_i. Hence, the current film thickness is $h = \lambda_2 H$. The film and substrate are perfectly bonded and both are incompressible so that they undergo the same deformation and $\lambda_1\lambda_2\lambda_3 = 1$.

The present model therefore represents the strictly incompressible limit for both constituents. It considers a dielectric film of finite thickness bonded to a semi-infinite substrate, and does not account for finite substrate thickness or compressibility-sensitive effects under strong confinement. The finite film thickness is retained explicitly in the bifurcation analysis, and no asymptotic thin-film approximation is invoked. As recently emphasized for thin layers, the incompressible and thin-layer limits need not commute [72]. Consequently, the present results should be interpreted within the strictly incompressible finite-thickness film/half-space setting; the effects of small but finite compressibility require a separate analysis.

The deformation originates from the prescribed mechanical pre-deformation along the x_1 and x_3 directions and the electric field induced within the film by the potential difference V across flexible electrodes deposited on its upper and lower surfaces, where the applied electric field can be represented by an Eulerian electric field vector $\mathbf{E} = [0, E_2, 0]^{\mathrm{T}}$, with the superscript $^{\mathrm{T}}$ standing for transpose. The associated Lagrangian field is $\mathbf{E}_L = [0, E_{L2}, 0]^{\mathrm{T}}$ with $E_{L2} = \lambda_2 E_2 = E_2/(\lambda_1\lambda_3)$. For the homogeneous deformed state, $E_2 = V/h$, and hence $E_{L2} = V/H$. In general, a soft dielectric film expands in its plane under a voltage. Although the calculations below focus on the plane-strain deformation, we first introduce the general triaxial energy density functions. To account for strain stiffening due to limited chain extensibility in both the substrate and film, we employ the Gent hyperelastic model for the substrate and the Gent ideal dielectric model for the film, so that their total free-energy density functions for a general triaxial deformation take the form

$$W_s = -\frac{\mu_s J_{ms}}{2}\ln\left(1 - \frac{I_1 - 3}{J_{ms}}\right),$$
$$W_f = -\frac{\mu_f J_{mf}}{2}\ln\left(1 - \frac{I_1 - 3}{J_{mf}}\right) - \frac{\varepsilon}{2} I_5, \tag{1}$$

respectively, where the μ_i $(i = s, f)$ are the initial elastic shear moduli in the absence of voltage, the J_{mi} $(i = s, f)$ are the Gent parameters, and ε is the film's electric permittivity, which remains unaffected by deformation. In Eq. (1), $I_1 = \mathrm{tr}\,\mathbf{C} = \lambda_1^2 + \lambda_2^2 + \lambda_3^2$ and $I_5 = \mathbf{E}_L \cdot \mathbf{C}^{-1}\mathbf{E}_L$, where $\mathbf{C} = \mathbf{F}^{\mathrm{T}}\mathbf{F}$ is the right Cauchy–Green deformation tensor and $\mathbf{F}$ is the deformation gradient tensor. The subscripts "s" and "f" refer to the physical quantities of the substrate and film, respectively.

For simplicity and to align with existing literature, we focus on the plane-strain deformation defined by $\lambda_1 = \lambda$, $\lambda_2 = \lambda^{-1}$, $\lambda_3 = 1$ in this study (note that in Section 2.2, we treat the general triaxial case). Here, λ denotes the prescribed pre-stretch: $\lambda > 1$ corresponds to tensile pre-stretch, $\lambda = 1$ to the undeformed state, and $\lambda < 1$ to pre-compression. This configuration is realized by constraining the system between two fixed, lubricated rigid plates normal to the x_3 direction and prescribing the in-plane pre-stretch $\lambda_1 = \lambda$ along the x_1 direction (see Fig. 2). The prescribed stretch λ is then held fixed while the voltage V is increased.

Under this plane-strain specialization, the corresponding energy density functions (1) can be written as follows:

$$W_s = -\frac{\mu_s J_{ms}}{2}\ln\left(1-\frac{\lambda^2+\lambda^{-2}-2}{J_{ms}}\right),$$
$$W_f = -\frac{\mu_f J_{mf}}{2}\ln\left(1-\frac{\lambda^2+\lambda^{-2}-2}{J_{mf}}\right)-\frac{1}{2}\varepsilon\lambda^2\frac{V^2}{H^2}. \tag{2}$$

When the soft dielectric film is under voltage V, the whole film–substrate system deforms homogeneously. Because the top surface at $x_2 = -h$ is free of electro-mechanical traction, the normal component of the total stress vanishes at this surface, while interfacial continuity implies that it also vanishes at the perfectly bonded interface $x_2 = 0$. Then, the following total Cauchy stress component along the x_1 direction is required to keep the plane-strain deformation in the film under voltage V and stretch λ:

$$\sigma_f = \frac{\mu_f J_{mf}(\lambda^2-\lambda^{-2})}{J_{mf}-\lambda^2-\lambda^{-2}+2}-\varepsilon\lambda^2(V/H)^2. \tag{3}$$

For the perfectly bonded film–substrate system, the prescribed stretch λ is maintained by external mechanical constraints, giving rise to generally nonzero in-plane reaction stresses. As the applied voltage increases, the tensile stress in a pre-stretched film progressively decreases and vanishes at a critical voltage V_0, while the in-plane stress in the substrate remains nonzero. Therefore, the condition $\sigma_f = 0$ is not imposed in the bilayer analysis. Under the special equilibrium state where the total Cauchy stress σ_f in the film along the x_1 direction vanishes (i.e., $\sigma_f = 0$), the corresponding dimensionless measure $\bar{E}_0 = \sqrt{\varepsilon/\mu_f}(V_0/H)$ of the voltage is

$$\bar{E}_0 = \sqrt{\frac{J_{mf}(\lambda_0^2-\lambda_0^{-2})}{(J_{mf}+2)\lambda_0^2-\lambda_0^4-1}}. \tag{4}$$

According to Eq. (1) and $J_{mf} > 0$, the Gent admissibility condition requires $1-(I_1-3)/J_{mf} > 0$, which gives $\lambda_0^2+\lambda_0^{-2}-2 < J_{mf}$. Moreover, requiring $\bar{E}_0$ to be a non-negative real number gives $\lambda_0 \geq 1$. Therefore, Eq. (4) is applicable to

$$1 \leq \lambda_0 < \left[\left(J_{mf}+2+\sqrt{J_{mf}^2+4J_{mf}}\right)/2\right]^{1/2}. \tag{5}$$

For $\lambda_0 < 1$, the Gent energy density functions remain admissible; however, Eq. (4) yields $\bar{E}_0^2 < 0$, rendering $\bar{E}_0$ non-real and thus physically inadmissible.

The expression for the corresponding stretch λ_0 in terms of $\bar{E}_0$ is too cumbersome to be presented explicitly here. In the neo-Hookean limit $J_{mf} \to \infty$, Eq. (4) reduces to $\bar{E}_0 = \sqrt{1-\lambda_0^{-4}}$ and then $\lambda_0 = (1-\bar{E}_0^2)^{-1/4}$, which recovers the classical result for ideal neo-Hookean dielectric films given in Ref. [3]. Eq. (4) describes the special equilibrium state corresponding to $\sigma_f = 0$ in the film and is not imposed as a constraint in the subsequent bonded film–substrate bifurcation analysis. In the bilayer problem, the prescribed stretch λ is held fixed while the applied voltage V is increased, and the critical instability voltage is determined from the full coupled incremental bifurcation condition.

2.2. Exact bifurcation equation

For the stability analysis, we adopt the theory of linearized incremental electro-elasticity [71,73] and the Stroh formalism [3,68]. We seek two-dimensional (2D) incremental solutions with a sinusoidal shape along the x_1 direction and amplitude variations along the x_2 direction, see Fig. 2(c).

Following a standard derivation procedure [3,68], the dimensionless incremental equilibrium equations are formulated into a first-order differential equation, $\boldsymbol{\eta}' = \mathrm{i}\mathbf{N}\boldsymbol{\eta}$, where $\boldsymbol{\eta} = [U_1 \;\; U_2 \;\; \Delta \;\; \Sigma_{21} \;\; \Sigma_{22} \;\; \Phi]^{\mathrm{T}}$ is the generalized displacement-traction Stroh vector, the prime denotes differentiation with respect to kx_2, $\mathbf{N}$ is the constant Stroh matrix, U_1, U_2, Δ, Σ_{21}, Σ_{22} and Φ are dimensionless functions of kx_2 only, k is the wrinkling wavenumber, U_1 and U_2 are the non-zero components of the incremental mechanical displacement vector, Δ is a measure of the incremental electric displacement in the x_2 direction, Σ_{21} and Σ_{22} are the non-zero components of a measure of the incremental mechanical traction vector on planes of constant x_2, and Φ is a measure of the incremental electric potential.

With solutions in the form $\boldsymbol{\eta}(kx_2) = \boldsymbol{\eta}^0 e^{\mathrm{i}qkx_2}$, the resulting eigenvalue problem $(\mathbf{N}-q\mathbf{I})\boldsymbol{\eta}^0 = \mathbf{0}$ provides three pairs of complex conjugate eigenvalues q_j and six eigenvectors $\boldsymbol{\eta}^{(j)}$ in the soft dielectric film ($-h \leq x_2 \leq 0$), with the general solution as

$$\boldsymbol{\eta}(kx_2) = \sum_{j=1}^{6} c_j \boldsymbol{\eta}^{(j)} e^{\mathrm{i}q_j kx_2}, \tag{6}$$

where c_j ($j = 1, \ldots, 6$) are arbitrary constants to be determined. The general incremental governing equations, Stroh matrices and characteristic equations are provided in Appendix.

To ensure general applicability, we consider a general homogeneous triaxial deformation characterized by the principal stretches $(\lambda_1, \lambda_2, \lambda_3)$, and derive the 3×3 submatrices of $\mathbf{N} = \begin{bmatrix}\mathbf{N}_1 & \mathbf{N}_2 \\ \mathbf{N}_3 & \mathbf{N}_1^{\mathrm{T}}\end{bmatrix}$ for the ideal Gent electro-elastic model given by Eq. $(1)_2$ as

$$\mathbf{N}_1 = \begin{bmatrix}0 & -1 & 0\\ -1 & 0 & 0\\ 0 & 0 & 0\end{bmatrix},\quad \mathbf{N}_2 = \begin{bmatrix}\lambda_1^2\lambda_3^2/(2\bar{W}_1) & 0 & \lambda_1^3\lambda_3^3\bar{E}_L/(2\bar{W}_1)\\ 0 & 0 & 0\\ \lambda_1^3\lambda_3^3\bar{E}_L/(2\bar{W}_1) & 0 & 1+\lambda_1^4\lambda_3^4\bar{E}_L^2/(2\bar{W}_1)\end{bmatrix},$$
$$\mathbf{N}_3 = \begin{bmatrix}N_{31} & 0 & 2\lambda_1\lambda_3\bar{E}_L\\ 0 & 2(\lambda_1^{-2}\lambda_3^{-2}-\lambda_1^2)\bar{W}_1+\lambda_1^2\lambda_3^2\bar{E}_L^2 & 0\\ 2\lambda_1\lambda_3\bar{E}_L & 0 & -1\end{bmatrix}, \tag{7}$$

where $\bar{E}_L = \sqrt{\varepsilon/\mu_f}\,E_{L2} = \sqrt{\varepsilon/\mu_f}(V/H)$ represents the dimensionless voltage, and

$$N_{31} = -\left[4\left(\lambda_1^2-\lambda_1^{-2}\lambda_3^{-2}\right)^2\bar{W}_{11}+2\left(\lambda_1^2+3\lambda_1^{-2}\lambda_3^{-2}\right)\bar{W}_1+3\lambda_1^2\lambda_3^2\bar{E}_L^2\right],$$
$$\bar{W}_1 = \frac{1}{2\left[1-\left(\lambda_1^2+\lambda_1^{-2}\lambda_3^{-2}+\lambda_3^2-3\right)/J_{mf}\right]},$$
$$\bar{W}_{11} = \frac{1}{2J_{mf}\left[1-\left(\lambda_1^2+\lambda_1^{-2}\lambda_3^{-2}+\lambda_3^2-3\right)/J_{mf}\right]^2}. \tag{8}$$

The Gent energy density function is admissible only when $1-(\lambda_1^2+\lambda_1^{-2}\lambda_3^{-2}+\lambda_3^2-3)/J_{mi} > 0$. Under plane-strain loading, this condition reduces to $J_{mi} > \lambda^2+\lambda^{-2}-2$. All numerical results reported below satisfy this condition. The eigenvalues $q_j = -q_{j+3} = \mathrm{i}p_j$ ($j = 1,2,3$) of $\mathbf{N}$ are

$$p_1 = \frac{1}{2}\left[\frac{(1+\lambda_1^2\lambda_3)\sqrt{\lambda_1^2\lambda_3^2+2\bar{W}_{11}(-1+\lambda_1^2\lambda_3)^2/\bar{W}_1}}{\lambda_1\lambda_3}+\frac{\sqrt{(1-\lambda_1^2\lambda_3)^2\left(\lambda_1^2\lambda_3^2+2\bar{W}_{11}(1+\lambda_1^2\lambda_3)^2/\bar{W}_1\right)}}{\lambda_1\lambda_3}\right],$$
$$p_2 = \frac{1}{2}\left[\frac{(1+\lambda_1^2\lambda_3)\sqrt{\lambda_1^2\lambda_3^2+2\bar{W}_{11}(-1+\lambda_1^2\lambda_3)^2/\bar{W}_1}}{\lambda_1\lambda_3}-\frac{\sqrt{(1-\lambda_1^2\lambda_3)^2\left(\lambda_1^2\lambda_3^2+2\bar{W}_{11}(1+\lambda_1^2\lambda_3)^2/\bar{W}_1\right)}}{\lambda_1\lambda_3}\right],$$
$$p_3 = 1, \tag{9}$$

which are positive real numbers, and the corresponding eigenvectors are the columns of the 6×3 matrix below:

$$\left[\boldsymbol{\eta}^{(1)}|\boldsymbol{\eta}^{(2)}|\boldsymbol{\eta}^{(3)}\right] = \begin{bmatrix}-\mathrm{i}p_1 & -\mathrm{i}p_2 & 0\\ 1 & 1 & 0\\ -\mathrm{i}\lambda_1\lambda_3 p_1\bar{E}_L & -\mathrm{i}\lambda_1\lambda_3 p_2\bar{E}_L & \mathrm{i}\\ \dfrac{2(1+p_1^2)\bar{W}_1}{\lambda_1^2\lambda_3^2}+\lambda_1^2\lambda_3^2\bar{E}_L^2 & \dfrac{2(1+p_2^2)\bar{W}_1}{\lambda_1^2\lambda_3^2}+\lambda_1^2\lambda_3^2\bar{E}_L^2 & \lambda_1\lambda_3\bar{E}_L\\ \dfrac{2\mathrm{i}(\lambda_1^4\lambda_3^2+p_1^2)\bar{W}_1}{p_1\lambda_1^2\lambda_3^2} & \dfrac{2\mathrm{i}(\lambda_1^4\lambda_3^2+p_2^2)\bar{W}_1}{p_2\lambda_1^2\lambda_3^2} & \mathrm{i}\lambda_1\lambda_3\bar{E}_L\\ -\lambda_1\lambda_3\bar{E}_L & -\lambda_1\lambda_3\bar{E}_L & -1\end{bmatrix}. \tag{10}$$

$$\mathbf{Z}=\begin{bmatrix} \left(\lambda_1^2\lambda_3^2\bar{E}_L^2+\dfrac{2\left(p_1+p_2\right)\bar{W}_1}{\lambda_1^2\lambda_3^2}\right) & -\mathrm{i}\left(\lambda_1^2\lambda_3^2\bar{E}_L^2+\dfrac{2\left(1-p_1p_2\right)\bar{W}_1}{\lambda_1^2\lambda_3^2}\right) & -\lambda_1\lambda_3\bar{E}_L \\ \mathrm{i}\left(\lambda_1^2\lambda_3^2\bar{E}_L^2+\dfrac{2\left(1-\lambda_1^4\lambda_3^2/p_1p_2\right)\bar{W}_1}{\lambda_1^2\lambda_3^2}\right) & \dfrac{2\left(p_1+p_2\right)\bar{W}_1\lambda_1^2}{p_1p_2} & -\mathrm{i}\lambda_1\lambda_3\bar{E}_L \\ -\lambda_1\lambda_3\bar{E}_L & \mathrm{i}\lambda_1\lambda_3\bar{E}_L & 1 \end{bmatrix}. \tag{11}$$

Box I.

The 6×6 complete matrix of eigenvectors is defined as $\mathcal{N}=\left[\boldsymbol{\eta}^{(1)}|\boldsymbol{\eta}^{(2)}|\boldsymbol{\eta}^{(3)}|\boldsymbol{\eta}^{(4)}|\boldsymbol{\eta}^{(5)}|\boldsymbol{\eta}^{(6)}\right]$, where the eigenvalues with negative imaginary parts are q_4, q_5, q_6 with associated eigenvectors $\boldsymbol{\eta}^{(4)}$, $\boldsymbol{\eta}^{(5)}$, $\boldsymbol{\eta}^{(6)}$, which are the complex conjugates of q_1, q_2, q_3 and $\boldsymbol{\eta}^{(1)}$, $\boldsymbol{\eta}^{(2)}$, $\boldsymbol{\eta}^{(3)}$, respectively.

For a soft dielectric material filling the entire half-space, the impedance matrix reads $\mathbf{Z}=-\mathrm{i}\mathbf{B}\mathbf{A}^{-1}$, where $\mathbf{A}$ and $\mathbf{B}$ are the 3×3 upper and lower submatrices in Eq. (10), respectively. For its explicit form, see Box I.

Accordingly, the bifurcation condition for Biot-type surface instability takes the form $\det\mathbf{Z}=0$ [74,75], or

$$2\bar{W}_1\left(p_1p_2-1\right)p_1p_2+2\lambda_1^4\lambda_3^2\bar{W}_1\left(1+p_1^2+p_1p_2+p_2^2\right)=p_1p_2\left(p_1+p_2\right)\lambda_1^4\lambda_3^4\bar{E}_L^2. \tag{12}$$

For the plane-strain deformation $\lambda_1=\lambda$, $\lambda_3=1$, the bifurcation condition Eq. (12) reduces to

$$2\bar{W}_1\left(p_1p_2-1\right)p_1p_2+2\lambda^4\bar{W}_1\left(1+p_1^2+p_1p_2+p_2^2\right)=p_1p_2\left(p_1+p_2\right)\lambda^4\bar{E}_L^2. \tag{13}$$

In the limit $J_m\to\infty$, this expression recovers the result from Wu et al. [3]. For equibiaxial stretching ($\lambda_1=\lambda_3=\lambda$), the same limiting case $J_m\to\infty$ yields the formula of Su et al. [68].

Here, the soft dielectric film has a finite thickness and is bonded to a hyperelastic half-space. At the interface $x_2=0$, the 3×1 dimensionless generalized traction $\mathbf{S}=[\Sigma_{21},\Sigma_{22},\Phi]^{\mathrm{T}}$ and displacement $\mathbf{U}=[U_1,U_2,\Delta]^{\mathrm{T}}$ satisfy the relation

$$\mathbf{S}_f(0)=\mathrm{i}\mathbf{Z}_f\mathbf{U}_f(0),\qquad \mathbf{S}_s(0)=\mathrm{i}\mathbf{Z}_s\mathbf{U}_s(0). \tag{14}$$

Perfect interfacial bonding imposes $\mathbf{U}_f(0)=\mathbf{U}_s(0)$ and $\mu_f\mathbf{S}_f(0)=\mu_s\mathbf{S}_s(0)$, which yields the exact bifurcation solution as

$$\det(\mathbf{Z}_f-r\mathbf{Z}_s)=0 \tag{15}$$

where $r=\mu_s/\mu_f$ is the substrate-to-film shear modulus ratio, and $\mathbf{Z}_f$, $\mathbf{Z}_s$ denote the impedance matrices of the soft dielectric film and substrate at $x_2=0$, respectively. This bifurcation equation (15) depends on the dimensionless quantities r, λ, kh, $\bar{E}_L$, J_{mf}, and J_{ms}.

For prescribed $(r,\lambda,J_{mf},J_{ms})$, Eq. (15) provides an exact implicit bifurcation condition for $\bar{E}_L$ as a function of the dimensionless wavenumber kh. The critical instability voltage is then determined numerically by minimizing the bifurcation voltage over kh. In contrast, Eq. (13) describes only the $kh\to\infty$ Biot-type surface-instability limit under plane-strain loading, whereas the finite-thickness film–half-space substrate results reported below are obtained from Eq. (15).

Here, with the film top face at $x_2=-h$ being traction-free and subjected to a fixed applied voltage, the interfacial impedance matrix of the film at $x_2=0$ is $\mathbf{Z}_f=-\mathrm{i}\mathbf{M}_3\mathbf{M}_1^{-1}$, where $\mathbf{M}_1,\mathbf{M}_3$ denote the 3×3 upper-diagonal and lower-off-diagonal submatrices of the 6×6 exponential matrix $\mathbf{M}=\exp(\mathrm{i}kh\mathbf{N})$. The latter admits the representation $\mathbf{M}=\mathcal{N}\boldsymbol{\Lambda}\mathcal{N}^{-1}$ when $\mathcal{N}$ is nonsingular, where $\boldsymbol{\Lambda}$ is diagonal with entries $e^{\mathrm{i}q_jkh}$ $(j=1,\ldots,6)$. For the hyperelastic substrate, the impedance matrix $\mathbf{Z}_s$ takes the form

$$\mathbf{Z}_s=\begin{bmatrix} -\mathrm{i}c_s(q_{s1}+q_{s2}) & -\mathrm{i}c_s(1+q_{s1}q_{s2}) & 0 \\ \mathrm{i}c_s(1+q_{s1}q_{s2}) & \mathrm{i}c_sq_{s1}q_{s2}(q_{s1}+q_{s2}) & 0 \\ 0 & 0 & 0 \end{bmatrix}, \tag{16}$$

where the roots $q_{sj}(j=1,2)$ are obtained from the following characteristic equation:

$$q_s^4+\frac{2b_s}{c_s}q_s^2+\frac{a_s}{c_s}=0, \tag{17}$$

with

$$a_s=2\lambda_1^2\bar{W}_{s1},\qquad b_s=\left(\lambda_1^{-2}\lambda_3^{-2}+\lambda_1^2\right)\bar{W}_{s1}+2\left(\lambda_1^2-\lambda_1^{-2}\lambda_3^{-2}\right)^2\bar{W}_{s11},$$
$$c_s=2\lambda_1^{-2}\lambda_3^{-2}\bar{W}_{s1}. \tag{18}$$

It is noted that q_{s1} and q_{s2} are the eigenvalues with positive imaginary parts, chosen such that $\exp(\mathrm{i}q_skx_2)$ decays into the substrate as $x_2\to+\infty$. For the admissible Gent substrate considered here, these roots are purely imaginary and can be written as $q_{sj}=\mathrm{i}p_{sj}(j=1,2)$, where $p_{sj}>0$ are the positive real numbers. Equivalently, the corresponding positive real numbers satisfy $p_s^4-(2b_s/c_s)p_s^2+a_s/c_s=0$.

This impedance matrix (16) is consistent with Eq. (11) for $\bar{E}_L=0$, provided that its last diagonal entry is set to zero to account for the 2D nature of the traction and displacement vectors in the hyperelastic substrate (with no electric field). Here, $\bar{W}_{s1}$ and $\bar{W}_{s11}$ are obtained by substituting J_{ms} for J_{mf} in the expressions for $\bar{W}_1$ and $\bar{W}_{11}$ from Eq. $(8)_{2,3}$, respectively.

2.3. Numerical post-buckling analysis

We use the finite element method to investigate the post-buckling behavior of the soft dielectric film–substrate system and validate the accuracy of the theoretical model.

The finite element simulations are performed under 2D plane-strain conditions using COMSOL Multiphysics® 6.2. The *Solid Mechanics* and *Electrostatics* physics interfaces are coupled through the *Electromechanical Forces* multiphysics feature. The mechanical response of the soft dielectric film is implemented using COMSOL's built-in incompressible Gent hyperelastic material model, with parameters μ_f and J_{mf} corresponding to the mechanical part of Eq. (2). The substrate follows either the incompressible Gent or neo-Hookean hyperelastic model, as specified for each parameter set. The electrical response is described by the *Electrostatics* interface with deformation-independent permittivity. Electromechanical forces are incorporated through the built-in coupling based on the Minkowski stress tensor, with electrostriction disabled.

Incompressibility in both constituents is enforced using a mixed displacement–pressure formulation, with an auxiliary pressure field introduced in each material domain. The computational domain is discretized using a free quadrilateral mesh. Quadratic serendipity shape functions are used for the displacement field, discontinuous linear Lagrange shape functions for the auxiliary pressure field, and quadratic interpolation for the electric potential. Reduced integration is not used.

The film–substrate system is modeled using a rectangular computational domain $[0,L_{\mathrm{cr}}]\times[-H,H_s]$ (see Fig. 3(a)), where L_{cr} is the width of the undeformed unit cell and represents the critical wavelength

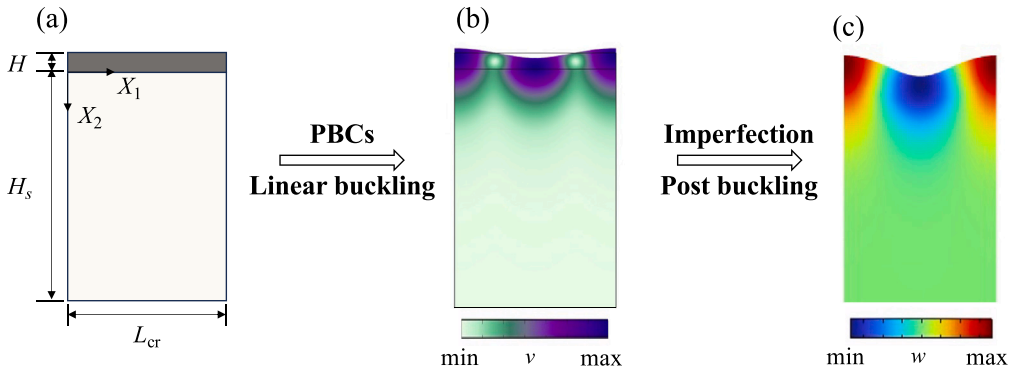


Fig. 3. Finite element calculation process. (a) Initial undeformed state: The film thickness is H, the substrate depth is H_s, and the width of the undeformed unit cell is set to the critical wrinkle wavelength L_{cr}. After applying the prescribed stretch λ, the unit-cell width becomes $l_{cr} = \lambda L_{cr}$, corresponding to the critical wrinkle wavelength in the current configuration; (b) Linear buckling mode: After applying PBCs, a linear buckling analysis is conducted to obtain the buckling mode, with the color contour representing the distribution of displacement mode v. (c) Post-buckling deformation mode: Introducing (b) as a geometric imperfection leads to the post-buckling stage, where the color contour represents the distribution of total displacement amplitude w.

of the wrinkling pattern in the undeformed configuration, H is the initial film thickness, and H_s is the initial depth of the substrate. After applying the prescribed stretch λ along the x_1 direction under plane-strain loading, the current wrinkle wavelength and substrate depth are $l_{cr} = \lambda L_{cr} = 2\pi/k_{cr}$ and $h_s = H_s/\lambda$, respectively.

For the plane-strain deformation in the X_1–X_2 plane, the prescribed stretch λ is imposed along the X_1 direction. The upper surface of the film is traction-free, while the lower surface of the substrate is fully constrained except in the horizontal x_1 direction. An electric potential is applied to both the upper and lower surfaces of the film, with a potential difference of V between them. On the left and right sides of the domain, we impose periodic boundary conditions (PBCs) to mimic the infinite layered half-space as

$$w_1(L_{cr}, X_2) - w_1(0, X_2) = (\lambda - 1)L_{cr}, \qquad w_2(L_{cr}, X_2) - w_2(0, X_2) = 0,$$
$$\phi(L_{cr}, X_2) - \phi(0, X_2) = 0, \tag{19}$$

where w_1 and w_2 represent the total displacements in the X_1 and X_2 directions, respectively, and ϕ is the total electric potential.

Then the numerical simulation is implemented in two sequential stages. In the first stage, a nonlinear stationary electro-mechanical solution at the prescribed stretch and applied voltage establishes the prestressed state, with the Gent constitutive response and electro-mechanical coupling retained. Linear buckling analysis is then performed about this state under the prescribed electro-mechanical PBCs in Eq. (19), and the resulting buckling mode (Fig. 3(b)) is adopted as the geometric imperfection for the subsequent nonlinear post-buckling analysis.

In the second stage, using this geometric imperfection for the soft dielectric film–substrate system subjected to the same electro-mechanical PBCs given in Eq. (19), we carry out nonlinear post-buckling analysis using stationary continuation with the applied voltage, or equivalently the dimensionless Lagrangian electric field $\bar{E}_L = \sqrt{\varepsilon/\mu_f}(V/H)$, as the control parameter. For fixed r, λ, and material parameters, $\bar{E}_L$ is increased with a prescribed increment $\Delta\bar{E}_L = 0.001$. At each voltage increment, the coupled displacement, auxiliary pressure, and electric-potential fields are solved using a fully coupled Newton method with automatic damping. The linearized systems at each Newton iteration are solved using the MUMPS direct solver. A relative solver tolerance of 10^{-3} and a maximum of 25 nonlinear iterations are specified for each voltage step. Arc-length continuation and branch switching are not employed. If nonlinear convergence cannot be achieved at a given voltage level, the parameter sweep is terminated. The reported paths are therefore restricted to equilibrium solutions obtained by voltage-controlled continuation; continuation through possible limit points and systematic tracing of additional branches are not undertaken. The resulting wrinkled morphology and displacement distribution are shown in Fig. 3(c), where the color contour represents the total displacement amplitude w.

3. Results and discussion

Because low-voltage actuation of dielectric elastomers is highly desirable for practical engineering applications [54], we investigate wrinkling evolution as the applied voltage V varies while the prescribed stretch λ is held fixed. Two configurations are adopted for the soft dielectric film–substrate system: (i) identical Gent parameters $J_{mf} = J_{ms} = J_m$ for the film and substrate, and (ii) distinct Gent parameters between the two layers.

We then plot the $\bar{E}_L$–kh bifurcation curves for a given shear modulus ratio $r = \mu_s/\mu_f$ and different prescribed values of λ. Typically (but not always) these curves exhibit a minimum, see Fig. 4, representing the critical voltage $\bar{E}_L^{cr}$ for wrinkling initiation, and we now quantify how strain stiffening modulates this critical value.

3.1. Identical Gent parameters

In this section, we consider $J_{mf} = J_{ms} = J_m$. The bifurcation curves of the dimensionless voltage $\bar{E}_L$ as a function of the wavenumber kh are presented in Fig. 4 for various values of the Gent parameter at six values of the prescribed stretch $\lambda = 2.0, 1.5, 1.2, 1.0, 0.9, 0.8$ and a fixed shear modulus ratio $r = \mu_s/\mu_f = 0.1$. In the limit $kh \to \infty$, all bifurcation curves converge to the root of Eq. (13). Notably, when $J_m = 1000$, our results achieve excellent agreement with Wu et al. [3], who used the neo-Hookean ideal dielectric model ($J_m \to \infty$). It is observed that the critical voltage $\bar{E}_L^{cr}$ decreases gradually as the prescribed stretch λ decreases, similar to the results reported by Wu et al. [3].

The results of Fig. 4 further reveal that the bifurcation curves of $\bar{E}_L$ with respect to kh generally exhibit non-monotonic behavior. All bifurcation curves exhibit a minimum, corresponding to the critical voltage $\bar{E}_L^{cr}$ of primary interest, except in Fig. 4(f), where the instability occurs mechanically, prior to the application of the voltage. In addition, as illustrated in Fig. 4(c)–(f) for small to modest pre-strains ($\lambda = 1.2, 1.0, 0.9, 0.8$), the bifurcation curves corresponding to different Gent parameters J_m overlap nearly completely, indicating that the Gent parameter J_m has negligible influence on the critical voltage required for wrinkling onset at these modest pre-strain levels. This is because, for modest pre-strains ($0.8 \le \lambda \le 1.2$), the Gent model behaves as the neo-Hookean model, leading to minimal deviations in the predicted critical voltage. For large tensile pre-stretches ($\lambda = 2.0$ and 1.5) in Fig. 4(a)–(b) and small J_m (e.g., $J_m = 10$, corresponding to pronounced strain

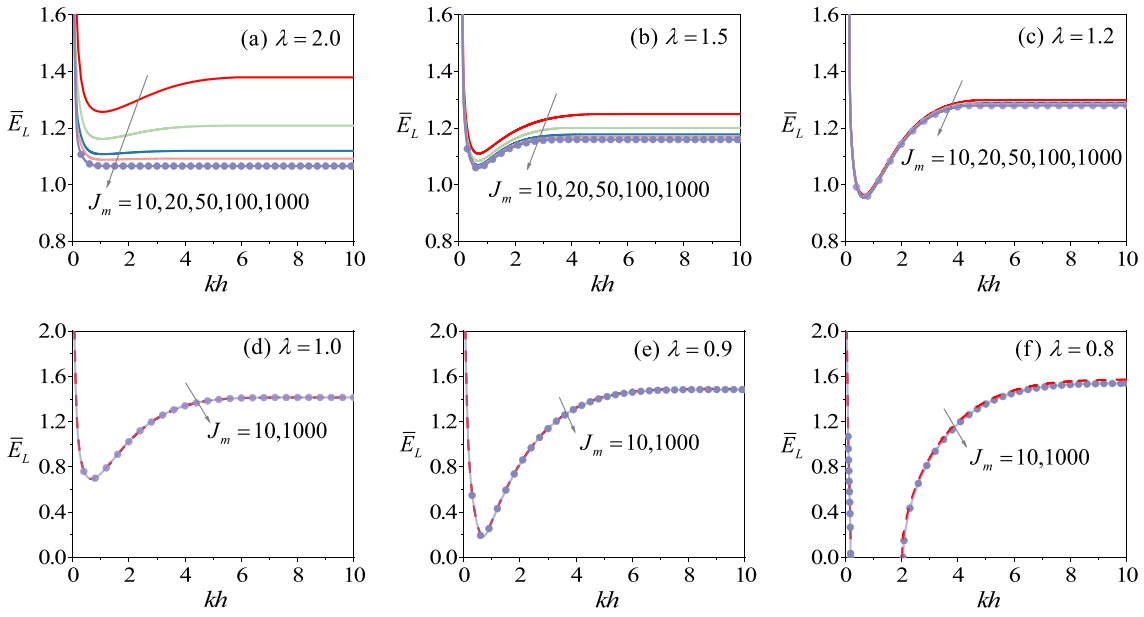


Fig. 4. Bifurcation curves of the dimensionless voltage $\bar{E}_L$ versus kh under a shear modulus ratio $r = \mu_s/\mu_f = 0.1$ and six values of the prescribed stretch λ: (a–c) tensile pre-stretches $\lambda = 2.0$, 1.5, and 1.2; (d) the undeformed state $\lambda = 1.0$; and (e–f) pre-compressions $\lambda = 0.9$ and 0.8 for different Gent parameters $J_m = 10, 1000$. The minima correspond to the critical voltage $\bar{E}_L^{\mathrm{cr}}$ and critical wavenumber $(kh)_{\mathrm{cr}}$. The circles denote predictions from Ref. [3], where the elastic behavior of both film and substrate follows the neo-Hookean ideal dielectric model.

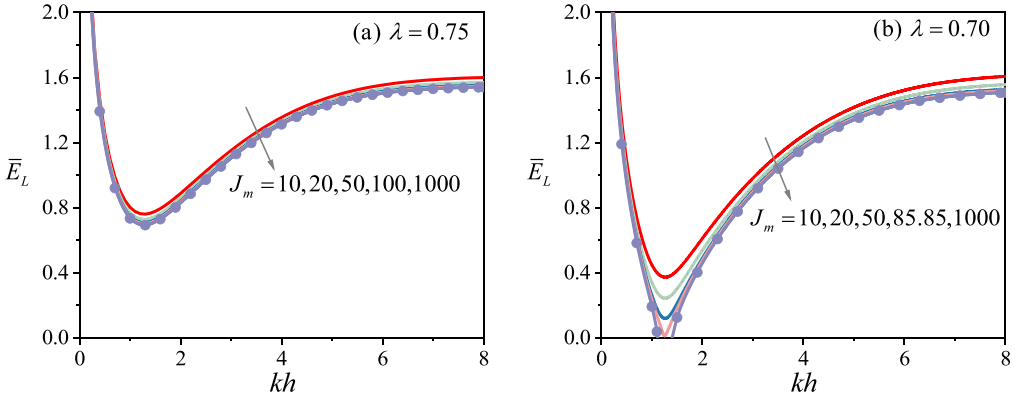


Fig. 5. Bifurcation curves of the dimensionless voltage $\bar{E}_L$ versus kh under a shear modulus ratio $r = \mu_s/\mu_f = 0.5$ and two fixed pre-compressions: (a) $\lambda = 0.75$ for various Gent parameters $J_m = 10, 20, 50, 100, 1000$; (b) $\lambda = 0.70$ for various Gent parameters $J_m = 10, 20, 50, 85.85, 1000$. The circles denote the neo-Hookean model predictions from Ref. [3].

stiffening), a distinct difference is observed between the bifurcation curves for $J_m = 10$ and $J_m = 1000$.

Previous work [3] has shown that increasing r requires stronger pre-compression to achieve low-voltage driving, and this stronger pre-compression can amplify the strain-stiffening effect governed by the Gent model. Consequently, Fig. 5 shows the bifurcation curves of the dimensionless voltage $\bar{E}_L$ as a function of kh for various Gent parameters under a shear modulus ratio $r = \mu_s/\mu_f = 0.5$ and contractile pre-stretches $\lambda = 0.75$ and 0.70. The Gent parameter noticeably affects the critical voltage $\bar{E}_L^{\mathrm{cr}}$, most clearly in Fig. 5(b): as J_m increases, the strain-stiffening effect weakens for the film–substrate system and $\bar{E}_L^{\mathrm{cr}}$ decreases. Moreover, Fig. 5(b) reveals a critical Gent parameter $J_{\mathrm{cr}} \simeq 85.85$ corresponding to the zero-critical-voltage boundary numerically obtained from Eq. (15) with $\bar{E}_L = 0$ and identical Gent parameters in the film and substrate. The critical Gent parameter J_{cr} is evaluated by locating the boundary between parameter sets with $\bar{E}_L^{\mathrm{cr}} = 0$ and those with a finite applied voltage. Thus, J_{cr} is not a universal material constant, but depends on the prescribed r and λ, i.e., $J_{\mathrm{cr}} = J_{\mathrm{cr}}(r, \lambda)$. When $J_m > J_{\mathrm{cr}}$, the strain-stiffening effect is insufficient to resist the pre-compression-driven instability, and the film–substrate system undergoes purely mechanical wrinkling prior to any applied voltage; when $J_m < J_{\mathrm{cr}}$, the pronounced finite-chain-extensibility significantly elevates the effective tangent stiffness, suppressing spontaneous wrinkling and requiring an additional electric-field-induced Maxwell stress to overcome this stiffening-enhanced structural resistance before wrinkling can be triggered. Physically, J_{cr} represents the balance point at which the finite-extensibility-induced stiffness gain exactly counteracts the destabilizing compressive driving force: above this threshold (weak stiffening), pre-compression alone governs the instability; below it (strong stiffening), the electric field becomes an indispensable additional driving mechanism. Failing to account for J_{cr} would therefore lead to a misjudgment of the wrinkling behavior at this parameter regime. To systematically examine how J_{cr} varies with λ and r, Fig. 6 maps the zero-critical-voltage boundaries.

Fig. 6(a)–(b) show the curves of the critical Gent parameter J_{cr} as a function of the prescribed stretch λ for two values of the shear modulus ratio $r = 0.1$ and 0.5. The black line represents the critical Gent parameter value J_{cr}, and the red line indicates the critical stretch

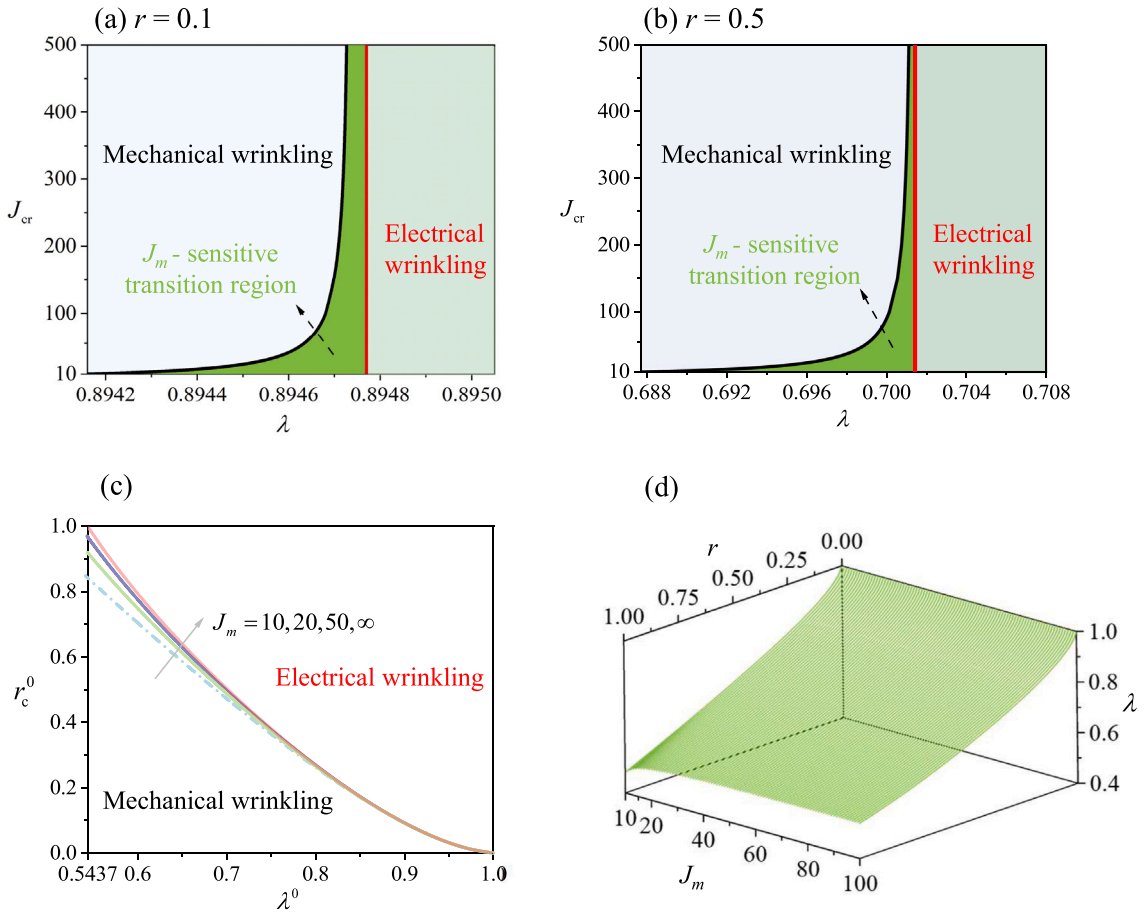


Fig. 6. (a,b) Critical Gent parameter J_{cr} as a function of λ for (a) $r = 0.1$ and (b) $r = 0.5$ (black curves). The red line indicates the critical stretch λ_c^0 for purely mechanical wrinkling in the neo-Hookean limit ($J_m \to \infty$). The shaded regions in (a) and (b) indicate mechanical wrinkling ($\lambda < \lambda_c^0$, $J_m > J_{cr}$), the J_m-sensitive transition region ($\lambda < \lambda_c^0$, $J_m < J_{cr}$), and electrical wrinkling ($\lambda > \lambda_c^0$). (c) $\lambda_c^0 - r_c^0$ critical curves for different Gent parameters $J_m = 10, 20, 50, \infty$, corresponding to zero critical voltage. The regions below and above the critical curves represent purely mechanical wrinkling and electrical wrinkling, respectively. (d) The 3D critical surface for purely mechanical wrinkling over the parameter range $r \in [0.0, 1.0]$, $\lambda \in [0.4, 1.0]$, and $J_m \in [10, 100]$.

λ_c^0, which is the critical value for the purely mechanical wrinkling instability of a neo-Hookean ($J_m \to \infty$) ideal dielectric film bonded to a hyperelastic substrate. Together, these two curves partition the parameter space into three instability regimes. When $\lambda < \lambda_c^0$ and $J_m > J_{cr}$, the system undergoes purely mechanical wrinkling without any applied voltage. When $\lambda < \lambda_c^0$ and $J_m < J_{cr}$, an electric field must be applied to trigger wrinkling, and the critical voltage depends sensitively on J_m. This region is referred to as the strain-stiffening-sensitive transition region or the J_m-sensitive transition region. When $\lambda > \lambda_c^0$ (electrical wrinkling region), wrinkling must be driven by voltage, regardless of the value of J_m. Meanwhile, this J_m-insensitivity in the electrical wrinkling regime admits a transparent physical interpretation. In the compressive regime of interest ($\lambda_c^0 < \lambda < 1$), the first invariant increment $I_1 - 3 = \lambda^2 + \lambda^{-2} - 2$ decreases monotonically from its maximum value at $\lambda = \lambda_c^0$ toward zero as $\lambda \to 1$. Throughout this regime, $(I_1 - 3)/J_m \ll 1$ for all Gent parameters of practical interest, so the Gent constitutive law reduces asymptotically to the neo-Hookean model, the finite-chain-extensibility constraint remains dormant, and J_m drops out of the bifurcation condition. By contrast, once λ drops below λ_c^0, $I_1 - 3$ grows rapidly and the ratio $(I_1 - 3)/J_m$ is no longer negligible: the Gent model deviates appreciably from its neo-Hookean limit, the finite-extensibility constraint is activated, and the critical voltage $\bar{E}_L^{cr}$ becomes strongly J_m-dependent.

Further, Fig. 6(c) presents the critical curves in the (λ_c^0, r_c^0) plane for different Gent parameters $J_{ms} = J_{mf} = J_m = 10, 20, 50, \infty$. Each curve corresponds to a vanishing critical voltage ($\bar{E}_L^{cr} = 0$) and therefore separates purely mechanical wrinkling from electrical wrinkling. When $r < r_c^0$ (or $\lambda < \lambda_c^0$), the system wrinkles mechanically before the application of voltage; when $r > r_c^0$ (or $\lambda > \lambda_c^0$), a finite voltage is required to trigger wrinkling instability. It is worth noting that the middle area between the two curves ($J_m = 10$ and ∞) shown in Fig. 6(c) is precisely the strain-stiffening-sensitive transition region ($\lambda < \lambda_c^0$ and $J_m < J_{cr}$) displayed in Fig. 6(a)–(b). As also shown in Fig. 6(c), r_c^0 increases monotonically with decreasing λ_c^0, indicating that stronger pre-compression expands the parameter r region for purely mechanical wrinkling. The effect of the Gent parameter is mainly visible in the strongly compressed regime ($\lambda \lesssim 0.7$). Specifically, as J_m decreases, the strain-stiffening effect becomes more pronounced and the critical curve $\lambda_c^0 - r_c^0$ shifts downward, implying that greater pre-compression or a smaller shear modulus ratio is required to induce purely mechanical wrinkling. In other words, as J_m decreases, the corresponding critical curves deviate further from the results of the neo-Hookean model. In contrast, the influence of strain stiffening becomes negligible in the weak-to-moderate pre-compression regime ($0.8 \le \lambda \le 1.0$), and all the critical curves exhibit excellent consistency. This demonstrates that when $0.8 \le \lambda \le 1.0$, using the neo-Hookean model in place of the Gent model does not incorrectly classify voltage-induced instabilities as purely mechanical instabilities.

Extending the 2D results in Fig. 6(a–c), (d) provides a 3D critical surface over the parameter range $r \in [0.0, 1.0]$, $\lambda \in [0.4, 1.0]$, and $J_m \in [10, 100]$. The continuous surface shows how the critical wrinkling boundary at $\bar{E}_L = 0$ evolves with λ, r, and J_m, capturing the

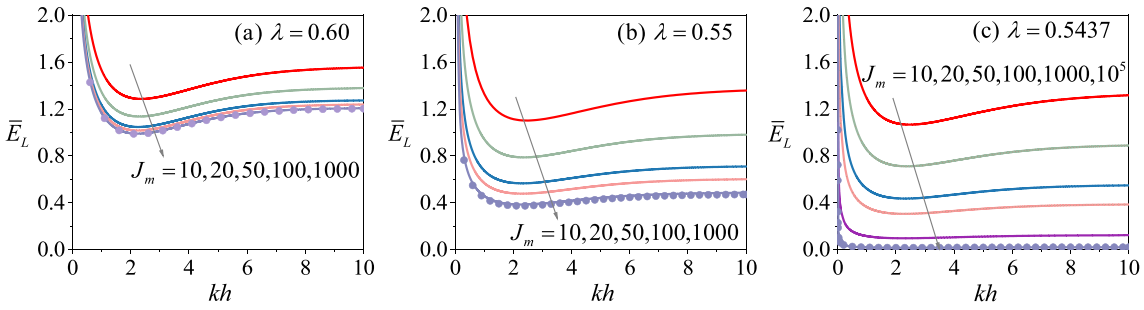


Fig. 7. Bifurcation curves of the dimensionless voltage $\bar{E}_L$ versus kh for a shear modulus ratio $r = \mu_s/\mu_f = 1.0$ and three prescribed pre-compressions: (a) $\lambda = 0.60$, (b) $\lambda = 0.55$, and (c) $\lambda = 0.5437$, with Gent parameters $J_m = 10, 20, 50, 100, 1000$ (and 10^5 for (c)). The circles denote the neo-Hookean limit ($J_m \to \infty$).

combined effects of the prescribed stretch λ and material parameters on the instability behavior. This comprehensive visualization serves as a direct reference for selecting operating conditions (purely mechanical or electro-mechanical) to obtain desired wrinkling modes in practical engineering. More importantly, it facilitates the avoidance of neglecting the strain-stiffening effect within the J_m-sensitive transition region, thus precluding misjudgments of the critical instability voltage: specifically, near the critical Gent parameter $J_{\rm cr}$, the omission of the strain-stiffening effect results in misclassifying stable systems as unstable. In other scenarios, neglecting the strain-stiffening effect tends to underestimate the critical voltage (see Fig. 5(a)).

When the soft dielectric film and hyperelastic substrate have the same initial elastic shear modulus ($r = 1.0$), Fig. 7 shows the bifurcation curves of the dimensionless voltage $\bar{E}_L$ as a function of kh for various Gent parameters and three pre-compressions $\lambda = 0.60, 0.55, 0.5437$, and highlights that the strain-stiffening effect on $\bar{E}_L^{\rm cr}$ is quite significant in this regime. It can be clearly seen that at a fixed value of λ, as J_m increases, the dimensionless critical voltage $\bar{E}_L^{\rm cr}$ gradually decreases. Specifically, at $\lambda = 0.55$ and $J_m = 10$, the dimensionless critical voltage $\bar{E}_L^{\rm cr} \simeq 1.10$. Nevertheless, the dimensionless critical voltage $\bar{E}_L^{\rm cr} \simeq 0.38$ when $\lambda = 0.55$ and $J_m = 1000$. It should be noted that the Biot limit for the neo-Hookean model of the hyperelastic half-space is about 0.543689, which is slightly less than 0.5437 in Fig. 7(c). Therefore, the result corresponding to Fig. 7(c) does not yet exhibit mechanical instability, and the corresponding critical voltage $\bar{E}_L^{\rm cr} > 0$. Note that soft dielectric film–substrate wrinkling is characterized by finite-wavelength minima in the bifurcation voltage at $(kh)_{\rm cr}$, determined by the film thickness, shear modulus ratio, and prescribed deformation. In contrast, for $r = 1$ with identical elastic constitutive responses in the two layers, the zero applied voltage mechanical problem approaches that of a homogeneous hyperelastic half-space. At this classical Biot limit, the surface instability is scale-free and does not select a unique physical wrinkle wavelength. Therefore, for $r = 1$ in the neo-Hookean limit, as λ approaches 0.543689 with $\bar{E}_L^{\rm cr} = 0$, the limiting wrinkling instability does not select a unique physical wavelength.

To more clearly observe the differences, we further demonstrate the evolutions of the critical voltage by plotting $\bar{E}_L^{\rm cr}$ versus the Gent parameter J_m at two representative shear modulus ratios $r = 0.5$ and $r = 1.0$ in Fig. 8. It also includes the numerical results obtained using COMSOL Multiphysics® (denoted by circles), allowing for a direct validation of the theoretical predictions against finite element simulations. For each prescribed combination of r, λ, and J_m, a nonlinear stationary solution of the flat configuration is first computed at each applied voltage under the electro-mechanical PBCs in Eq. (19). The resulting state is used in a coupled prestressed eigenfrequency analysis, with the electro-mechanical coupling retained in the linearized problem. The FEM critical voltage is identified as the voltage at which the squared eigenfrequency of the relevant wrinkling mode reaches zero from positive values [76]. The calculations use $H_s/L_{\rm cr} = 10$ and characteristic mesh sizes of $L_{\rm cr}/20$ in both the film and substrate, consistent with the convergence results in Section 3.3. It can be clearly seen that as J_m increases, the critical voltage $\bar{E}_L^{\rm cr}$ decreases significantly. The truncation point of the abscissa in Fig. 8(a), denoted by a blue star, corresponds to the result shown in Fig. 5(b), which is the critical Gent parameter $J_{\rm cr} \approx 85.85$. It is worth noting from Fig. 8(a) that for $\lambda = 0.7$ and $r = 0.5$, when $J_m < J_{\rm cr} = 85.85$, the film–substrate system requires an additional voltage to trigger the wrinkling instability. When $J_m \geq J_{\rm cr} = 85.85$, the system has undergone purely mechanical instability, which is a completely different type of instability. For $\lambda = 0.75$ and $r = 0.5$ in Fig. 8(a), the critical voltage converges to the neo-Hookean ideal dielectric result (dashed line). Similarly, for $\lambda = 0.5437$, 0.55, and 0.6 with $r = 1.0$ in Fig. 8(b), the critical voltage $\bar{E}_L^{\rm cr}$ converges to the neo-Hookean values of 0.0158, 0.37340, and 0.98651, respectively.

Moreover, as the prescribed stretch λ decreases, corresponding to increasing pre-compression, the transition Gent parameter $J_{\rm tran}$ at which the Gent model prediction begins to deviate from the neo-Hookean result becomes larger. Note that $J_{\rm tran}$ is different from the previously mentioned zero-critical-voltage instability threshold $J_{\rm cr}$ and is defined as a conservatively selected transition value of J_m above which the relative deviation of the dimensionless critical voltage $\delta = \left|\bar{E}_L^{\rm cr} - \bar{E}_{L,\rm NH}^{\rm cr}\right| / \bar{E}_{L,\rm NH}^{\rm cr} \leq 5\%$ when $\bar{E}_{L,\rm NH}^{\rm cr} > 0$. Here, $\bar{E}_L^{\rm cr}$ and $\bar{E}_{L,\rm NH}^{\rm cr}$ denote the dimensionless critical voltages predicted by the Gent and neo-Hookean ideal dielectric models, respectively. Thus, $J_{\rm tran}$ provides a practical criterion for when the neo-Hookean approximation is sufficiently accurate. Specifically, the transition values are approximately $J_{\rm tran} \simeq 100$, 610, and 10^6 for $r = 1$ and $\lambda = 0.60$, 0.55, and 0.5437, respectively, as shown in Fig. 8(b). Therefore, when J_m exceeds the corresponding transition value ($J_m \gtrsim J_{\rm tran}$), the neo-Hookean model provides an accurate approximation to the Gent model. Conversely, when J_m falls below this threshold ($J_m \lesssim J_{\rm tran}$), the strain-stiffening effect becomes non-negligible, and the Gent model should be adopted. For $\lambda = 0.5437$, although $\bar{E}_{L,\rm NH}^{\rm cr}$ remains finite, its near-zero value makes the relative deviation ill-conditioned and may artificially amplify the apparent discrepancy. Therefore, the corresponding absolute difference $\Delta = \left|\bar{E}_L^{\rm cr} - \bar{E}_{L,\rm NH}^{\rm cr}\right|$ is also reported below for this case.

To further quantify the effect of strain stiffening on the critical voltage, Fig. 9(a) illustrates the evolution of the absolute deviation in the critical voltage, defined as $\Delta = \left|\bar{E}_L^{\rm cr} - \bar{E}_{L,\rm NH}^{\rm cr}\right|$, with respect to J_m for $r = 1.0$ and $\lambda = 0.60$, 0.55, and 0.5437. A pronounced dependence of the critical voltage on the Gent parameter is observed. Fig. 9(b) further presents the evolution of the relative deviation in the critical voltage δ as a function of J_m. For $\lambda = 0.5437$, 0.55, and 0.60, the relative deviations in the critical voltage at $J_m = 10$ are 66.35, 1.95, and 0.30, respectively. Because $\bar{E}_{L,\rm NH}^{\rm cr}$ is small at $\lambda = 0.5437$, the relative deviation is ill-conditioned and should be interpreted together with the absolute deviation in Fig. 9(a).

Moreover, Fig. 10 shows the relationship of the dimensionless critical voltage $\bar{E}_L^{\rm cr}$ and the corresponding dimensionless critical wavenumber $(kh)_{\rm cr}$ with the shear modulus ratio r for two pre-compression levels, $\lambda = 0.70$ and 0.55, with different Gent parameters $J_m = 10$, 50, and ∞. In all cases, a critical threshold value $r_{\rm c}^0$ exists, consistent with

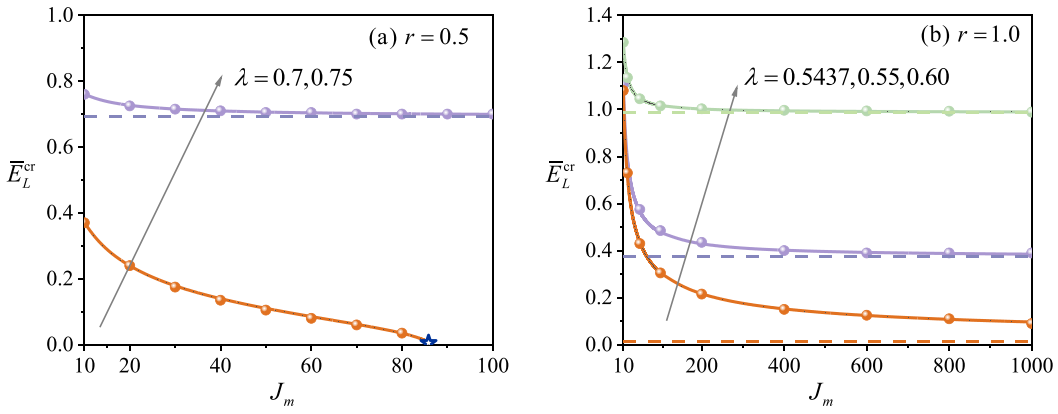


Fig. 8. (a) Dimensionless critical voltage $\bar{E}_L^{cr}$ versus J_m for $r = 0.5$ and pre-compressions $\lambda = 0.70$ and 0.75; (b) $\bar{E}_L^{cr}$ versus J_m for $r = 1.0$ and pre-compressions $\lambda = 0.5437$, 0.55, and 0.60. Circles denote finite-element results obtained using COMSOL Multiphysics®. The dashed line indicates the neo-Hookean limit ($J_m \to \infty$).

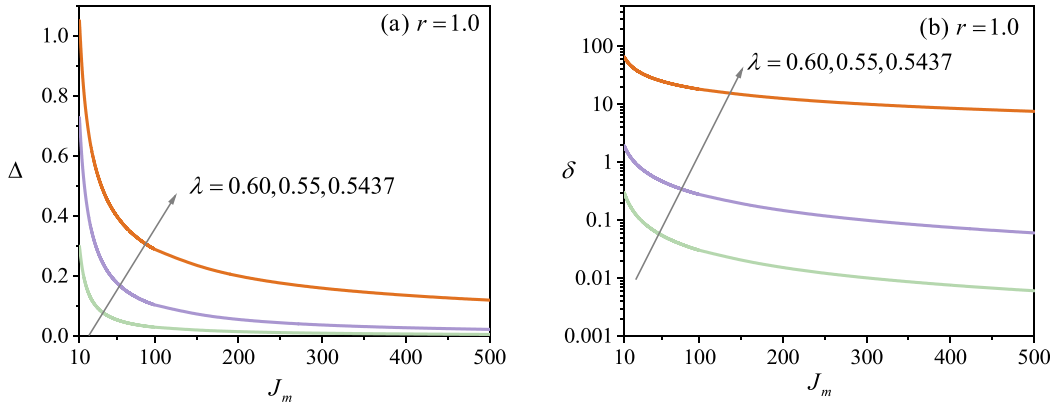


Fig. 9. Variations of the (a) absolute deviation Δ and (b) relative deviation δ of the dimensionless critical voltage $\bar{E}_L^{cr}$ with respect to J_m for $r = 1.0$ and $\lambda = 0.60$, 0.55, and 0.5437.

the results shown in Fig. 6(c). Electro-mechanical wrinkling instability can be triggered only for $r > r_c^0$, whereas purely mechanical wrinkling occurs for $r \le r_c^0$. For a fixed J_m, the critical voltage rises monotonically with increasing r, implying that a larger shear modulus ratio between the two layers enhances the resistance against electro-mechanical wrinkling. Meanwhile, under the pre-compression $\lambda = 0.70$ in Fig. 10(a), the curves for $J_m = 50$ and $J_m \to \infty$ remain very close to each other. Nevertheless, a distinguishable gap occurs between $J_m = 10$ and $J_m \to \infty$. This indicates that the strain-stiffening effect is prominent for relatively small J_m ($J_m < 50$), whereas the predictions gradually converge to the neo-Hookean results as J_m increases. In contrast, under strong pre-compression $\lambda = 0.55$, all curves separate evidently, indicating a much stronger strain-stiffening effect. Consequently, the neo-Hookean model ($J_m \to \infty$) is no longer an appropriate approximation for strongly compressed cases; otherwise, the critical voltage would be underestimated. Fig. 10(c) and (d) show the corresponding critical wavenumber $(kh)_{cr}$. For a fixed λ and Gent parameter J_m, $(kh)_{cr}$ increases with the shear modulus ratio r. At $\lambda = 0.70$, the three $(kh)_{cr}$ curves nearly overlap, indicating that strain stiffening has only a weak effect on the critical wavelength. Under the stronger pre-compression $\lambda = 0.55$, decreasing J_m leads to an increase in $(kh)_{cr}$ over the common electrically induced-wrinkling range. Mechanically, the critical wavenumber or wavelength reflects the combined interplay among the strain stiffening J_m, the shear modulus ratio r, and the prescribed pre-stretch λ.

Overall, for the identical-Gent configuration ($J_{mf} = J_{ms} = J_m$) within the investigated range $r \in [0, 1]$, stronger pre-compression is required to induce wrinkling as r approaches unity. Consequently, the influence of strain stiffening on the critical voltage becomes increasingly significant. Accordingly, the Gent model is recommended as the default constitutive model for quantitative material screening and device stability evaluation, thereby avoiding substantial underestimation of the critical voltage that may arise from the neo-Hookean approximation of the elastic response within this parameter regime.

3.2. Distinct Gent parameters

The benchmark analyses presented above were conducted by assuming identical Gent parameters for the film and substrate, i.e., $J_{ms} = J_{mf} = J_m$. To further elucidate the role of material nonlinearity, we first consider the case with $J_{mf} \to \infty$ and varying J_{ms}. It is found that variations in J_{ms} primarily affect the instability behavior through the substrate, whose strain-stiffening-induced structural resistance dominates the response of the film–substrate system. The resulting trends are qualitatively consistent with those discussed in Section 3.1. Therefore, this case is not presented separately for brevity. Instead, we focus on the complementary case with $J_{ms} \to \infty$ and varying J_{mf}.

Fig. 11 shows the bifurcation curves of the dimensionless voltage $\bar{E}_L$ as a function of kh for various Gent parameters J_{mf} when $r = \mu_s/\mu_f = 1.0$ and $\lambda = 0.60, 0.55$. It is observed that, as J_{mf} decreases, the strain-stiffening effect becomes more prominent and $\bar{E}_L^{cr}$ decreases instead of increasing as in Section 3.1. Physically, increased strain stiffening of the film renders the film–substrate system more susceptible to wrinkling. This is because a smaller J_{mf} corresponds to a stronger strain-stiffening effect, which enhances the effective stiffness of the film when subjected to pre-compression. Consequently, as J_{mf} decreases, the effective instantaneous elastic modulus ratio r_{eff} of the substrate

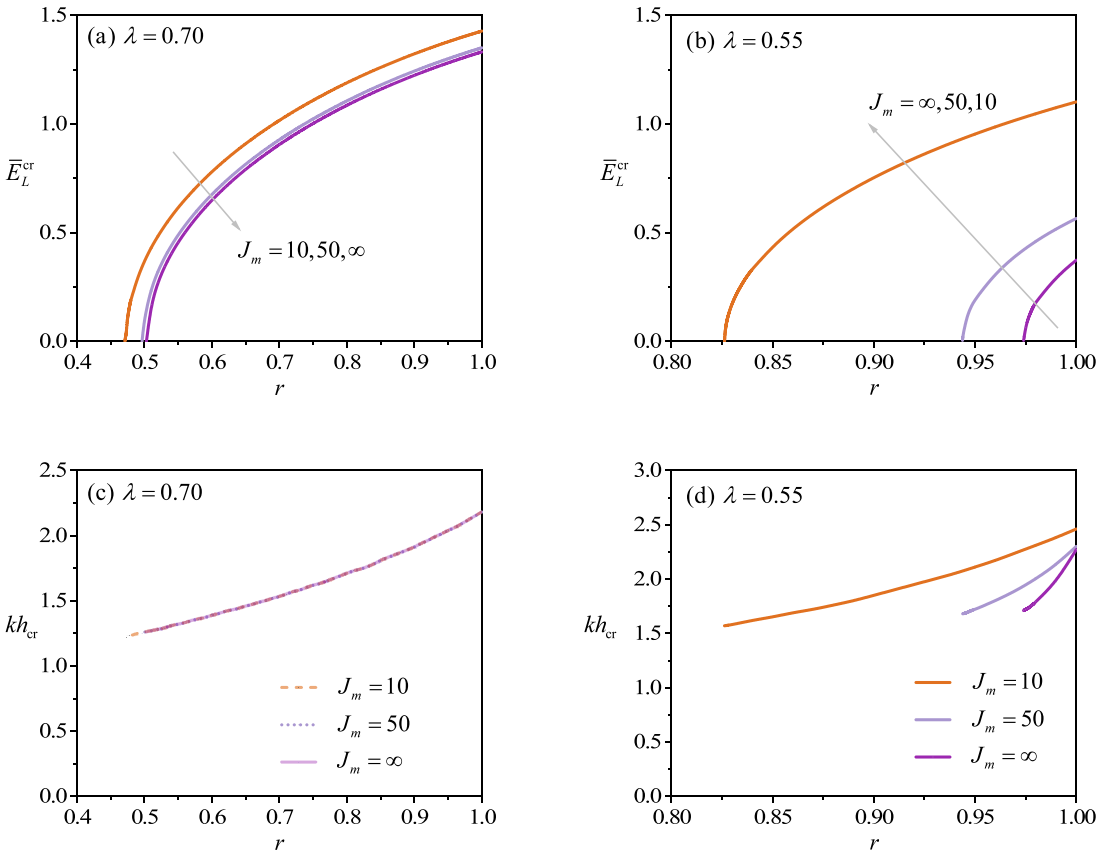


Fig. 10. Dimensionless critical voltage $\bar{E}_L^{cr}$ (a,b) and dimensionless critical wavenumber $(kh)_{cr}$ (c,d) versus the shear modulus ratio r for J_m = 10, 50, and ∞ at two levels of pre-compression: (a,c) $\lambda = 0.70$; (b,d) $\lambda = 0.55$. The corresponding dimensionless wrinkle wavelength is $l_{cr}/h = 2\pi/(kh)_{cr}$.

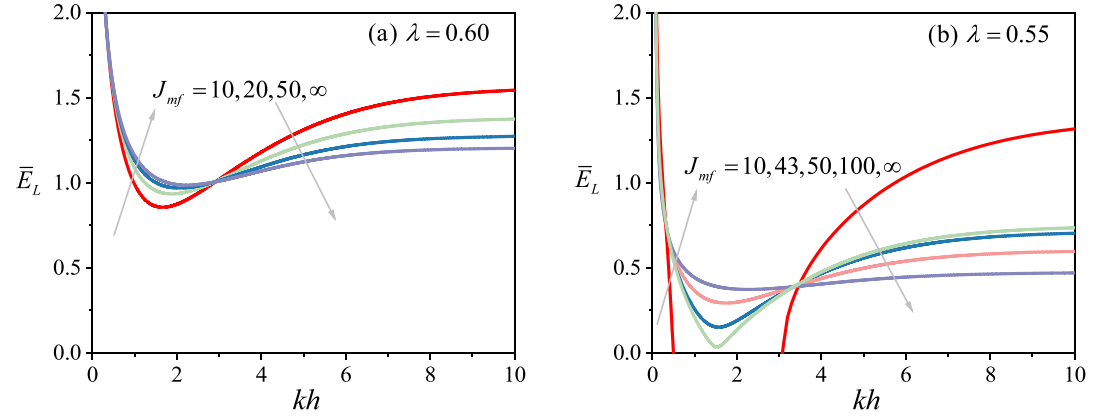


Fig. 11. Bifurcation curves of the dimensionless voltage $\bar{E}_L$ versus kh under a shear modulus ratio $r = \mu_s/\mu_f = 1.0$ for two fixed pre-compressions: (a) $\lambda = 0.60$ with various Gent parameters $J_{mf} = 10, 20, 50, \infty$ for the soft dielectric film; (b) $\lambda = 0.55$ with various Gent parameters $J_{mf} = 10, 43, 50, 100, \infty$ for the film, while the hyperelastic substrate follows the neo-Hookean model.

to the film, defined in Eq. (21), decreases, thereby making the system more susceptible to wrinkling instability [3]. Moreover, Fig. 11(b) clearly demonstrates that a critical Gent parameter $J_{cr}^f \simeq 43$ also exists: when $J_m > J_{cr}^f$, an applied voltage is required to trigger wrinkling; when $J_m < J_{cr}^f$, the system undergoes purely mechanical wrinkling without any applied voltage. Failing to account for J_{cr}^f would therefore result in an incorrect prediction of the wrinkling behavior in this parameter regime.

To clarify the physical significance of the effective instantaneous modulus ratio r_{eff}, we evaluate the representative instantaneous elastic moduli $\mathcal{A}_{02222}^{(f)}$ and $\mathcal{A}_{02222}^{(s)}$ of the Gent film and neo-Hookean substrate, respectively, using Eqs. (A.5) and (A.14) in Appendix. The corresponding dimensionless instantaneous elastic moduli are

$$\bar{\mathcal{A}}_{02222}^{(f)} = \frac{\mathcal{A}_{02222}^{(f)}}{\mu_f} = \frac{\lambda^{-2}}{\eta_f} + \frac{2\lambda^{-4}}{J_{mf}\eta_f^2} + \lambda^2 \bar{E}_L^2, \qquad \bar{\mathcal{A}}_{02222}^{(s)} = \frac{\mathcal{A}_{02222}^{(s)}}{\mu_s} = \lambda^{-2}, \tag{20}$$

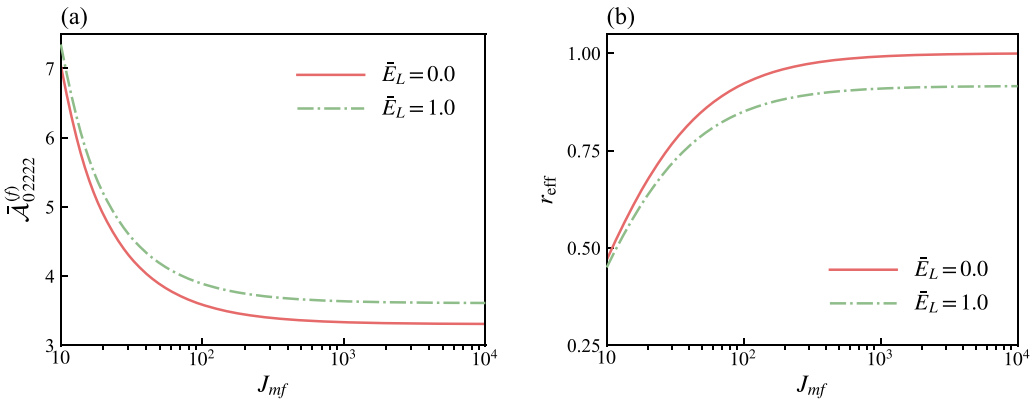


Fig. 12. (a) Dimensionless instantaneous elastic modulus $\bar{\mathcal{A}}^{(f)}_{02222}$ of the film and (b) dimensionless effective instantaneous elastic modulus ratio r_{eff} as functions of J_{mf} for a Gent film bonded to a neo-Hookean substrate, with $r = 1.0$, $\lambda = 0.55$, and $\bar{E}_L = 0.0$ and 1.0.

where $\eta_f = 1 - (\lambda^2 + \lambda^{-2} - 2)/J_{mf}$. The final term in $\bar{\mathcal{A}}^{(f)}_{02222}$ represents the electric-field contribution. The pre-stress induced by pre-stretching is reflected in the instantaneous moduli through their dependence on λ. Using these instantaneous moduli in Eq. (20), we define the effective instantaneous elastic modulus ratio as

$$r_{\text{eff}} = \frac{\mathcal{A}^{(s)}_{02222}}{\mathcal{A}^{(f)}_{02222}} = r\,\frac{\bar{\mathcal{A}}^{(s)}_{02222}}{\bar{\mathcal{A}}^{(f)}_{02222}}, \tag{21}$$

which indicates that although the initial shear modulus ratio r remains constant during electro-mechanical loading, r_{eff} depends on the prescribed pre-stretch, the electric field, and the Gent parameter.

Fig. 12 shows the variations of the dimensionless instantaneous film modulus $\bar{\mathcal{A}}^{(f)}_{02222}$ and the effective instantaneous elastic modulus ratio r_{eff} with J_{mf} for a Gent film bonded to a neo-Hookean substrate at $r = 1.0$ and $\lambda = 0.55$, with $\bar{E}_L = 0.0$ and 1.0. As shown in Fig. 12(a), decreasing J_{mf} increases the dimensionless instantaneous film modulus at both electric-field levels. Since the dimensionless instantaneous modulus of the neo-Hookean substrate is independent of J_{mf}, this increase in the film modulus leads to a decrease in r_{eff}, as shown in Fig. 12(b). These results quantitatively support the preceding interpretation that a smaller J_{mf} reduces r_{eff}, making the film–substrate system more susceptible to wrinkling instability [3].

To systematically characterize how J^f_{cr} varies with λ and r, Fig. 13 maps the zero-critical-voltage boundaries. Fig. 13(a) plots the critical Gent parameter J^f_{cr} of the soft dielectric film versus the prescribed stretch λ for $r = 1.0$. The black line represents the critical Gent parameter J^f_{cr} of the film, and the red line represents the Biot-limit critical stretch $\lambda^0_c(r = 1) \simeq 0.54369$ for purely mechanical wrinkling in the neo-Hookean limit ($J_{mf} \to \infty$). Together, these two curves partition the parameter space into different instability regimes. When $\lambda < \lambda^0_c$ for any value of J_{mf}, or when $\lambda > \lambda^0_c$ with $J_{mf} < J^f_{\text{cr}}$ (i.e., within the strain-stiffening-sensitive transition region), the system undergoes purely mechanical wrinkling without any applied voltage. By contrast, in the electrical wrinkling region where $\lambda > \lambda^0_c$ and $J_{mf} > J^f_{\text{cr}}$, an external electric field is required to trigger the wrinkling instability.

Similar to Figs. 6(c), 13(b) presents the critical curves in the (λ^0_c, r^0_c) plane corresponding to $\bar{E}^{\text{cr}}_L = 0$ for different film Gent parameters $J_{mf} = 10, 20, \infty$. As shown in Fig. 13(b), the region below the critical curve corresponds to purely mechanical wrinkling prior to voltage application, whereas the region above the curve requires a finite applied voltage to trigger wrinkling instability. It is observed that a smaller J_{mf}, associated with stronger strain stiffening in the film, shifts the critical curve upward in the (λ^0_c, r^0_c) plane, indicating that the purely mechanical wrinkling can be achieved with weaker pre-compression or a larger shear modulus ratio. Consequently, the critical curves progressively deviate from the neo-Hookean prediction as J_{mf} decreases.

Building upon the 2D results presented in Fig. 13(a)–(b), (c) further extends the analysis to a 3D critical surface spanning the parameter space $r \in [0.0, 1.0]$, $\lambda \in [0.4, 1.0]$, and $J_{mf} \in [10, 100]$. The continuous surface illustrates the evolution of the critical wrinkling boundary at $\bar{E}_L = 0$ with respect to λ, r, and J_{mf}, thereby capturing the coupled effects of pre-compression and material parameters on the instability behavior.

It is worth noting that the two cases in Sections 3.1 and 3.2 yield opposite errors when the strain-stiffening effect is neglected, a contrast rooted in which layer dominates the wrinkling behavior. In Case (i) ($J_{mf} = J_{ms} = J_m$), the semi-infinite substrate dominates the overall structural stiffness. A smaller J_m stiffens the entire system, raising its resistance to out-of-plane buckling and thereby *increasing* $\bar{E}^{\text{cr}}_L$. The neo-Hookean approximation therefore *underestimates* the critical voltage, erroneously classifying stable configurations as unstable. In Case (ii) ($J_{ms} \to \infty$), strain stiffening acts on the film alone. A smaller J_{mf} renders the bilayer more susceptible to wrinkling, thereby *decreasing* $\bar{E}^{\text{cr}}_L$. The neo-Hookean approximation therefore *overestimates* the critical voltage, erroneously classifying unstable configurations as stable. In both scenarios, neglecting strain stiffening under large tensile pre-stretch or strong pre-compression leads to a systematic misclassification of stability states and unreliable quantitative predictions for soft dielectric film–substrate systems.

Table 1 quantifies the relative errors δ of the critical voltage $\bar{E}^{\text{cr}}_L$ for the film–substrate system under different constitutive models at $r = 1.0$ and $\lambda = 0.60, 0.55$. Note that for each constituent described by the Gent model, the corresponding Gent parameter is set to 10, i.e., $J_m = 10$. It is observed that the relative error of Case (i) increases to 195.0% at $\lambda = 0.55$. More importantly, at $\lambda = 0.55$, Case (ii) predicts purely mechanical wrinkling without any applied voltage ($\bar{E}_L = 0$), whereas the neo-Hookean model predicts that an additional electric voltage is still required to trigger wrinkling. This discrepancy indicates a fundamental misjudgment of the wrinkling mechanism, namely confusing purely mechanically induced wrinkling with voltage-induced wrinkling, rather than merely a quantitative discrepancy in the predicted critical voltage.

3.3. Post-buckling analysis by the finite element method

Before examining the post-buckling response, we assess convergence with respect to substrate depth and film-mesh resolution, as well as sensitivity to the initial geometric imperfection, using representative cases with $r = 0.1$ and $\lambda = 1.00$, 0.95, and 0.90. The system consists of a Gent soft dielectric film ($J_{mf} = 10$) bonded to a neo-Hookean substrate ($J_{ms} \to \infty$). The eigenmode-scaling factor κ_{FEM} controls the magnitude of the initial imperfection. It is fixed at 1.0 in the substrate-depth and film-mesh convergence studies and varied in the imperfection-sensitivity study. For these comparisons, the FEM critical

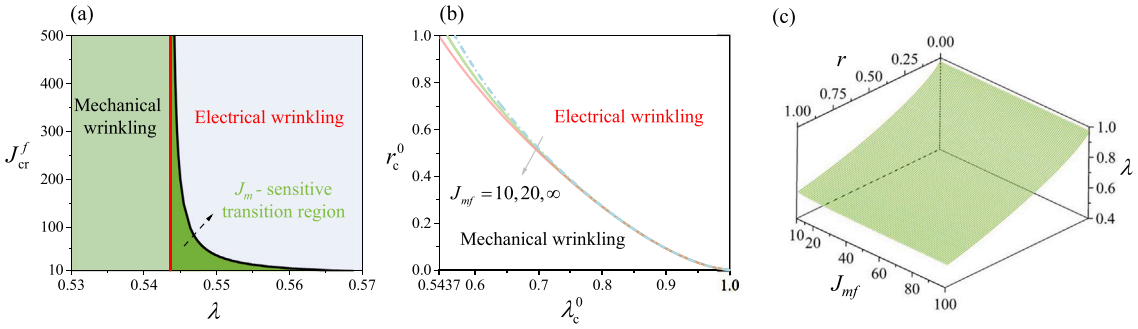


Fig. 13. (a) Critical Gent parameter J_{cr}^f of the soft dielectric film as a function of λ (black curve) for $r = 1.0$, when the substrate is characterized by the neo-Hookean model ($J_{ms} \to \infty$). The red line indicates the critical stretch λ_c^0 for purely mechanical wrinkling in the neo-Hookean limit ($J_{mf} \to \infty$). The shaded regions indicate mechanical wrinkling ($\lambda < \lambda_c^0$ for any value of J_{mf}), the strain-stiffening-sensitive transition region ($\lambda > \lambda_c^0$, $J_{mf} < J_{cr}^f$), and electrical wrinkling ($J_{mf} > J_{cr}^f$). (b) $\lambda_c^0 - r_c^0$ critical curves for different Gent parameters $J_{mf} = 10, 20, \infty$ corresponding to zero critical voltage. The region below the critical curve corresponds to purely mechanical wrinkling prior to voltage application, whereas the region above the curve requires a finite applied voltage to trigger wrinkling instability. (c) The 3D critical surface for purely mechanical wrinkling over the parameter range $r \in [0.0, 1.0]$, $\lambda \in [0.4, 1.0]$, and $J_{mf} \in [10, 100]$.

Table 1
Comparison of the relative error $\delta = \left|\bar{E}_L^{cr} - \bar{E}_{L,NH}^{cr}\right| / \bar{E}_{L,NH}^{cr}$ in the critical voltage $\bar{E}_L^{cr}$ for the film–substrate system under different constitutive models at $r = 1.0$ and $\lambda = 0.60, 0.55$.

λ	Case	$\bar{E}_L^{cr}$	$\bar{E}_{L,NH}^{cr}$	δ	Direction of error
0.60	(i) Gent film + Gent substrate	1.28604	0.98651	30.4%	Underestimate
	(ii) Gent film + neo-Hookean substrate	0.85624	0.98651	13.2%	Overestimate
0.55	(i) Gent film + Gent substrate	1.10149	0.37340	195.0%	Underestimate
	(ii) Gent film + neo-Hookean substrate	Wrinkled	0.37340	Misjudgment	Overestimate

Note: "Wrinkled" indicates that purely mechanical wrinkling instability emerges without applied voltage. "Misjudgment" represents an incorrect classification of the instability mode (purely mechanical wrinkling or electro-mechanical wrinkling) rather than a quantitative error in the predicted critical voltage.

Table 2
Convergence of the FEM-calculated dimensionless critical voltage $\bar{E}_{L,FEM}^{cr}$ with respect to the substrate-depth-to-critical-wrinkle-wavelength ratio H_s/L_{cr}. The characteristic mesh size is fixed at $L_{cr}/20$ in both the soft dielectric film and substrate, with $r = 0.1$ and $\kappa_{FEM} = 1.0$.

	$H_s/L_{cr} = 10$	$H_s/L_{cr} = 20$	$H_s/L_{cr} = 40$
$\lambda = 0.90$	0.1707	0.1707	0.1707
$\lambda = 0.95$	0.5326	0.5326	0.5328
$\lambda = 1.00$	0.6911	0.6911	0.6911

Table 3
Convergence of the FEM-calculated dimensionless critical voltage $\bar{E}_{L,FEM}^{cr}$ with respect to film-mesh refinement for $H_s/L_{cr} = 10$ and $\kappa_{FEM} = 1.0$, with the characteristic substrate mesh size fixed at $L_{cr}/20$.

	$L_{cr}/10$	$L_{cr}/20$	$L_{cr}/40$
$\lambda = 0.90$	0.1707 ($N_f = 2$)	0.1707 ($N_f = 2$)	0.1707 ($N_f = 4$)
$\lambda = 0.95$	0.5326 ($N_f = 2$)	0.5326 ($N_f = 2$)	0.5328 ($N_f = 4$)
$\lambda = 1.00$	0.6911 ($N_f = 2$)	0.6911 ($N_f = 2$)	0.6911 ($N_f = 5$)

voltage $\bar{E}_{L,FEM}^{cr}$ is estimated from the post-buckling curves at $\xi = \Delta y/H = 0.05$, where Δy is the difference between the maximum and minimum vertical coordinates of points on the free surface, and H is the initial thickness of the soft dielectric film.

The influence of substrate depth H_s should be evaluated relative to the wrinkle wavelength [77,78]. Accordingly, Table 2 examines the effect of the constrained bottom boundary on the critical voltage by varying the ratio H_s/L_{cr} from 10 to 20 and 40, while keeping the characteristic mesh size at $L_{cr}/20$ in both the film and substrate and all other numerical settings unchanged for each parameter set. Here, L_{cr} denotes the critical wrinkle wavelength in the undeformed configuration. Compared with the case of $H_s/L_{cr} = 10$, increasing this ratio to 20 or 40 changes the FEM critical voltage $\bar{E}_{L,FEM}^{cr}$ by less than 0.04%. This negligible variation supports the use of $H_s/L_{cr} = 10$ for the subsequent numerical analysis.

In addition to the substrate-depth convergence study, we examine the convergence of the FEM-calculated dimensionless critical voltage with respect to film-mesh refinement. Because relatively few elements are used through the film thickness, the analysis focuses on refining the film mesh while keeping the substrate mesh size fixed at $L_{cr}/20$. The characteristic film-mesh size is set to $L_{cr}/10$, $L_{cr}/20$, and $L_{cr}/40$. The corresponding minimum number of quadrilateral elements through the film thickness, N_f, is reported in Table 3. For each mesh configuration, the film and substrate meshes share nodes along their common interface. As shown in Table 3, refining the film mesh from $L_{cr}/20$ to $L_{cr}/40$ increases the minimum number of elements through the film thickness from $N_f = 2$ to $N_f = 4$ or 5, while changing the critical voltage by no more than 0.04%. With the substrate mesh size held fixed, these results indicate that the post-buckling-based critical-voltage estimate is relatively insensitive to further film-mesh refinement for the cases examined. Accordingly, a characteristic mesh size of $L_{cr}/20$ is adopted for both the film and substrate in the subsequent post-buckling simulations.

We further assess the sensitivity of the dimensionless critical voltage to the initial geometric imperfection. The imperfection is introduced based on the first linear-buckling mode as $\mathbf{X}_{imp} = \mathbf{X} + \kappa_{FEM}\mathbf{u}_{eig,1}$, where $\mathbf{X}$ and $\mathbf{X}_{imp}$ denote the position vectors of the initially flat and imperfect configurations, respectively, and $\mathbf{u}_{eig,1}$ is the displacement field associated with the first linear-buckling eigenmode. The eigenmode-scaling factor κ_{FEM} is specified through COMSOL's built-in *Geometric Imperfection* feature. The dimensionless initial imperfection amplitude

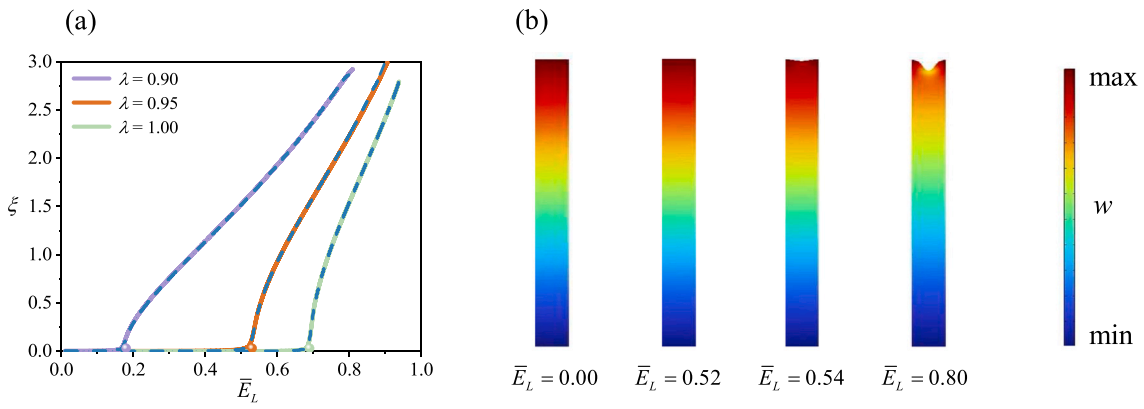


Fig. 14. (a) Bifurcation diagrams showing the dimensionless wrinkling amplitude ξ versus the dimensionless applied voltage $\bar{E}_L$ for $r = 0.1$ and $\lambda = 0.90, 0.95, 1.00$, with $J_{mf} = 10$ for the soft dielectric film and the neo-Hookean model ($J_{ms} \to \infty$) for the substrate. The dashed lines denote the case where the elastic responses of both the film and substrate obey the neo-Hookean model, i.e., $J_{mf} = J_{ms} = J_m \to \infty$, and the dots indicate the critical wrinkling voltages predicted by the linearized stability theory. (b) Contour plots of the deformed configurations for $\bar{E}_L = 0.00, 0.52, 0.54, 0.80$ at $\lambda = 0.95$. The color bar denotes the total displacement magnitude w.

Table 4
Sensitivity of the FEM-calculated dimensionless critical voltage $\bar{E}^{\mathrm{cr}}_{L,\mathrm{FEM}}$ to the eigenmode-scaling factor κ_{FEM} for $H_s/L_{\mathrm{cr}} = 10$. The characteristic mesh size is fixed at $L_{\mathrm{cr}}/20$ in both the soft dielectric film and substrate, with $r = 0.1$.

	$\kappa_{\mathrm{FEM}} = 0.5$	$\kappa_{\mathrm{FEM}} = 1.0$	$\kappa_{\mathrm{FEM}} = 2.0$
$\lambda = 0.90$	0.1735	0.1707	0.1650
$\lambda = 0.95$	0.5334	0.5326	0.5312
$\lambda = 1.00$	0.6914	0.6911	0.6903

is defined as $\xi_0 = \Delta y_0/H$, where Δy_0 is the peak-to-valley height of the initially imperfect free surface. Table 4 shows that the dimensionless critical voltage $\bar{E}^{\mathrm{cr}}_{L,\mathrm{FEM}}$ decreases with increasing κ_{FEM}, reflecting the effect of larger initial geometric imperfections. Relative to $\kappa_{\mathrm{FEM}} = 0.5$, increasing the factor to 1.0 and 2.0 changes the critical voltage by at most 1.61% and 4.90%, respectively. The case $\kappa_{\mathrm{FEM}} = 2.0$ is included to assess the effect of a larger initial imperfection. For the subsequent post-buckling simulations, we adopt $\kappa_{\mathrm{FEM}} = 1.0$ as the default setting because it introduces a small initial imperfection, with $\xi_0 \lesssim 10^{-4}$ in the cases examined, while yielding critical-voltage estimates close to those obtained with $\kappa_{\mathrm{FEM}} = 0.5$.

Using the numerical settings specified above, we now examine the post-buckling response by plotting the dimensionless amplitude of the free-surface wrinkles, $\xi = \Delta y/H$, as a function of the dimensionless voltage $\bar{E}_L$ for $r = 0.1$ and $\lambda = 0.90$, 0.95, and 1.00. The film is described by the Gent ideal dielectric model with $J_{mf} = 10$, and the substrate is described by the neo-Hookean model ($J_{ms} \to \infty$). We present the results in Fig. 14(a), where the solid curves correspond to the finite element results and the dots indicate the critical wrinkling voltages predicted by the theoretical analysis.

Fig. 14(a) shows that stronger pre-compression (smaller λ) corresponds to a lower critical voltage. Physically, increasing pre-compression produces a more strongly compressed base state, so that less additional Maxwell loading is required to reach the bifurcation condition. Accordingly, the dimensionless critical voltage $\bar{E}^{\mathrm{cr}}_L$ decreases as λ decreases. All post-buckling curves exhibit a monotonically increasing wrinkling amplitude ξ, indicating a smooth and continuous post-buckling response beyond the critical voltage, consistent with supercritical-like behavior. Meanwhile, the dashed lines in Fig. 14(a) represent the case where the elastic parts of both the film and the substrate follow the neo-Hookean model, i.e., $J_{mf} = J_{ms} = J_m \to \infty$. As seen from the dashed lines, the strain-stiffening effect exhibits a negligible influence on the bifurcation curves for weak pre-compression ($0.9 \lesssim \lambda \leq 1.0$), which is consistent with the conclusions presented in Section 3.1.

Moreover, Fig. 14(a) demonstrates that the post-buckling analysis accurately predicts the theoretical critical voltage at the onset of initial wrinkling, which is further confirmed by finite-element post-buckling deformation contours in Fig. 14(b). For $\lambda = 0.90$, 0.95, and 1.00 with $r = 0.1$, the corresponding critical voltages are approximately $\bar{E}^{\mathrm{cr}}_L = 0.18$, 0.53, and 0.69, respectively. Furthermore, Fig. 14(b) presents deformation contour maps of the soft dielectric film–substrate system with $r = 0.1$ and $\lambda = 0.95$ for $\bar{E}_L = 0.00, 0.52, 0.54, 0.80$. The results indicate a monotonic increase in the wrinkling amplitude with increasing voltage. A clear post-buckling evolution is observed: the system remains essentially flat at $\bar{E}_L = 0.52$ but develops pronounced wrinkling at $\bar{E}_L = 0.54$. This transition is in good agreement with the theoretical critical voltage $\bar{E}^{\mathrm{cr}}_L = 0.53$.

To further highlight the influence of the strain-stiffening effect, we examine the case where both the elastic energy components of the film and substrate share identical Gent parameters $J_{mf} = J_{ms} = J_m = 10, 20, 50$, with $r = 0.5$ and $\lambda = 0.7$, as presented in Fig. 15(a). The results demonstrate that the strain-stiffening effect becomes increasingly pronounced as pre-compression intensifies with decreasing λ. Fig. 15(a) clearly shows that the post-buckling wrinkling response at $\lambda = 0.7$ is smooth and supercritical-like, with the critical voltage decreasing as J_m increases, in good agreement with the foregoing theoretical analysis illustrated in Section 3.1.

For the stronger pre-compression case ($\lambda = 0.6$, $r = 1.0$), the finite element results in this regime exhibit a qualitatively different post-buckling character from those at moderate pre-compression ($\lambda = 0.7$). We provide typical results under strong pre-compression ($\lambda = 0.6$, $r = 1.0$) in Fig. 15(b), which includes three sets of constitutive combinations for the elastic responses: (i) both the film and substrate follow the Gent model with $J_{mf} = J_{ms} = 10$; (ii) the film adopts the Gent model and the substrate follows the neo-Hookean model with $J_{mf} = 10, J_{ms} \to \infty$; and (iii) the reference case where both the film and substrate obey the neo-Hookean model with $J_{mf} = J_{ms} \to \infty$.

Fig. 15(b) demonstrates that the three curves exhibit a rapid increase in the wrinkle amplitude after the onset of wrinkling. In addition, the distinct horizontal shift of the critical voltage $\bar{E}^{\mathrm{cr}}_L$ among different constitutive cases clearly demonstrates that the Gent parameter exerts a remarkable influence. Specifically, for Case (i) ($J_{mf} = J_{ms} = 10$), the critical voltage exceeds that of the full neo-Hookean Case (iii). This is because the overall system becomes stiffer, with the substrate dominating the wrinkling instability behavior, which

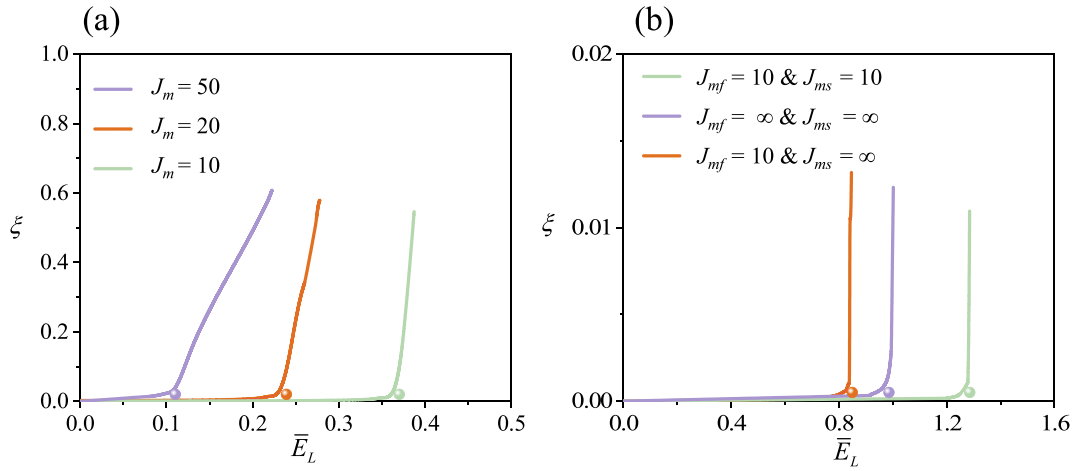


Fig. 15. Bifurcation diagrams showing the dimensionless wrinkling amplitude ξ versus the dimensionless applied voltage $\bar{E}_L$: (a) $r = 0.5$ and $\lambda = 0.7$ with $J_{mf} = J_{ms} = J_m = 10, 20, 50$; (b) $r = 1.0$ and $\lambda = 0.6$ under different constitutive combinations of J_{mf} and J_{ms} describing the elastic responses. The dots indicate the critical wrinkling voltage as predicted by the linearized stability theory.

enhances the resistance to wrinkling instability and thus increases the critical voltage.

By contrast, for Case (ii) ($J_{mf} = 10, J_{ms} = \infty$), the critical voltage is lower than that of the full neo-Hookean Case (iii). All these observations are qualitatively consistent with the numerical results presented in Sections 3.1 and 3.2.

Moreover, Figs. 14 and 15 demonstrate that the wrinkle amplitude increases markedly once the critical voltage is reached. However, due to the presence of initial geometric imperfections, the amplitude evolution initiates from a value close to zero rather than from an ideal zero-deflection state. Even under moderate and strong pre-compression conditions with $\lambda = 0.7$ and 0.6, the predicted critical voltages remain in close agreement with the theoretical values, further validating the accuracy of the present theoretical framework.

The reported post-buckling paths represent equilibrium solutions obtained through voltage-controlled continuation. For the weak-to-moderate pre-compression cases considered, smooth post-buckling responses are traced as the applied voltage increases. Under strong pre-compression, however, further analysis, including arc-length continuation and weakly nonlinear analysis [79,80], is required to resolve possible limit points and rigorously characterize the observed sharp transition. It remains unclear whether this transition corresponds to a genuine subcritical bifurcation or arises from other mechanisms, a question left open for future investigations.

4. Conclusions

We presented a theoretical and numerical analysis of the electro-mechanical wrinkling instability of a soft dielectric film bonded to a hyperelastic substrate, incorporating strain stiffening in either or both layers under combined electrical and mechanical loading. Using the Stroh formulation and the surface impedance matrix method, we derived exact analytical solutions for the wrinkling bifurcation of the film–substrate system.

For the two representative constitutive combinations examined, critical Gent parameters (J_{cr} for Case (i), where both the elastic constitutive responses of the soft dielectric film and substrate obey the Gent model with identical Gent parameters, and J_{cr}^{f} for Case (ii), where the film follows the Gent ideal dielectric model and the substrate follows the neo-Hookean model) divide the parameter space into distinct wrinkling regimes governed by the prescribed stretch λ and shear modulus ratio r. Ignoring strain-stiffening effects and these critical thresholds renders the conventional neo-Hookean description for the elastic constituents of the film–substrate system incapable of properly distinguishing between mechanical and electrical wrinkling transitions, leading to qualitative misjudgment of stability modes and substantial quantitative deviations in the critical triggering voltage. Furthermore, a 3D critical mechanical-wrinkling surface spanning the parameter space of the Gent parameter J_m, prescribed stretch λ, and shear modulus ratio r is established, together with the $\lambda_c^0 - r_c^0$ critical curves for different Gent parameters corresponding to zero critical voltage.

Finally, numerical finite-element analyses in COMSOL Multiphysics® validate the developed theoretical predictions for the electro-mechanical wrinkling of dielectric film–substrate systems across different prescribed stretch and shear modulus ratio combinations. Under weak-to-moderate pre-compression ($0.8 \lesssim \lambda \leq 1.0$), the system exhibits a supercritical-like post-buckling response, as a rising applied voltage induces continuous growth of the wrinkling amplitude (with the strain-stiffening effect remaining negligible at weak pre-compression, consistent with the preceding theoretical analysis). By contrast, strong pre-compression ($\lambda = 0.6$) induces wrinkling behavior marked by a rapid increase in the wrinkling amplitude at the critical voltage. Moreover, the Gent parameter exerts a prominent modulation effect on the critical voltage magnitude, as the full Gent-Gent configuration (Case (i)) yields a higher critical voltage when strain stiffening acts in both constituents, while the Gent-film/neo-Hookean-substrate layout (Case (ii)) reduces the critical voltage value through a decreased effective instantaneous elastic modulus ratio. Furthermore, the computed equilibrium branches can be tracked over the reported range for smooth, supercritical-like post-buckling responses. However, tracing possible additional equilibrium branches under strong pre-compression would require advanced path-following algorithms, which are beyond the scope of the present study.

Thus, our findings not only identify the feasible parameter window for controllable and reversible voltage-triggered wrinkling but also establish critical parameter boundaries within the assumptions of the present model. The analytical framework and finite-element results presented herein provide a mechanics-based reference for understanding the effects of strain stiffening and constitutive behavior under electro-mechanical loading. They may also motivate future experimental investigations and exploration of potential applications in low-voltage actuation, soft robotics, flexible electronics, and

bioinspired functional systems. Experimental validation of the effects of the Gent parameter on wrinkling and post-buckling behavior remains an objective for future work.

CRediT authorship contribution statement

Linghao Kong: Writing – original draft, Visualization, Validation, Software, Methodology, Formal analysis, Data curation, Conceptualization. **Liang Si:** Visualization, Validation, Software. **Renwei Mao:** Writing – review & editing. **Michel Destrade:** Writing – review & editing, Supervision, Methodology, Conceptualization. **Bin Wu:** Writing – review & editing, Validation, Supervision, Project administration, Methodology, Funding acquisition, Conceptualization.

Declaration of competing interest

The authors declare that they have no known competing financial interests or personal relationships that could have appeared to influence the work reported in this paper.

Appendix. Incremental governing equations, Stroh matrices, and characteristic equations

This appendix presents the incremental formulations for the principal deformation and normal electric field considered in the main text, including the incremental governing equations, Stroh matrices, and associated characteristic equations for the soft electro-elastic film and hyperelastic substrate. We refer the interested reader to the works by [68,69,71].

For the incompressible electro-elastic film, the incremental equilibrium equation, incremental incompressibility constraint, incremental Gauss law, and incremental electric field-potential relation are

$$\dot{T}^{(f)}_{0pi,p}=0,\qquad u^{(f)}_{i,i}=0,\qquad \dot{D}^{(f)}_{Li,i}=0,\qquad \dot{E}^{(f)}_{Li}=-\dot{\phi}^{(f)}_{,i}, \tag{A.1}$$

where $\dot{\mathbf{T}}^{(f)}_0$, $\dot{\mathbf{D}}^{(f)}_L$, and $\dot{\mathbf{E}}^{(f)}_L$ denote the push-forward increments in nominal stress, Lagrangian electric displacement, and Lagrangian electric field, respectively. The quantities $\mathbf{u}^{(f)}$ and $\dot{\phi}^{(f)}$ are the incremental displacement vector and electric potential.

The total energy density function $W_f(\mathbf{F},\mathbf{E}_L)$ in Eq. (1) uses the Lagrangian electric field vector $\mathbf{E}_L$ as the independent electrical variable. To change the independent variable from $\mathbf{E}_L$ to the Lagrangian electric displacement vector $\mathbf{D}_L$, we introduce the Legendre-transformed energy density function $\Omega_f(\mathbf{F},\mathbf{D}_L)$ as

$$\Omega_f(\mathbf{F},\mathbf{D}_L)=W_f(\mathbf{F},\mathbf{E}_L)+\mathbf{E}_L\cdot\mathbf{D}_L. \tag{A.2}$$

The electric constitutive relations associated with the two electro-elastic energy density functions are

$$\mathbf{D}_L=-\frac{\partial W_f}{\partial \mathbf{E}_L},\qquad \mathbf{E}_L=\frac{\partial \Omega_f}{\partial \mathbf{D}_L}. \tag{A.3}$$

Substituting the Gent ideal dielectric model (1) into Eq. (A.3)$_1$ and using the relation $\mathbf{E}_L=\mathbf{F}^{\mathrm{T}}\mathbf{E}$ yields $\mathbf{D}=\varepsilon\mathbf{E}$, where $\mathbf{D}=\mathbf{F}\mathbf{D}_L$ is the Eulerian electric displacement vector. Hence, $\mathbf{E}_L=\varepsilon^{-1}\mathbf{C}\mathbf{D}_L$. Using this relation, the Legendre-transformed energy density function for the Gent ideal dielectric model becomes

$$\Omega_f(\mathbf{F},\mathbf{D}_L)=-\frac{\mu_f J_{mf}}{2}\ln\left(1-\frac{I_1-3}{J_{mf}}\right)+\frac{1}{2\varepsilon}\mathbf{D}_L\cdot\mathbf{C}\mathbf{D}_L. \tag{A.4}$$

This $\mathbf{D}_L$-based representation in Eq. (A.4) is an equivalent Legendre-transformed description of the $\mathbf{E}_L$-based representation defined by Eq. (1). Using $\Omega_f(\mathbf{F},\mathbf{D}_L)$, the instantaneous electro-elastic modulus tensors of the soft dielectric film are defined as

$$\begin{aligned}&\mathcal{A}^{(f)}_{0pkqj}=F_{p\alpha}F_{q\beta}\frac{\partial^2\Omega_f}{\partial F_{k\alpha}\partial F_{j\beta}},\quad \Gamma^{(f)}_{0pkq}=F_{p\alpha}F^{-1}_{\beta q}\frac{\partial^2\Omega_f}{\partial F_{k\alpha}\partial D_{L\beta}},\\ &K^{(f)}_{0pq}=F^{-1}_{\alpha p}F^{-1}_{\beta q}\frac{\partial^2\Omega_f}{\partial D_{L\alpha}\partial D_{L\beta}}.\end{aligned} \tag{A.5}$$

For an isotropic electro-elastic material under the principal deformation and normal electric field considered here, the Stroh matrix of the soft electro-elastic film is written in non-dimensional form as

$$\mathbf{N}=\begin{bmatrix} 0 & \frac{\tau_{22}}{c}-1 & 0 & \frac{1}{c} & 0 & -\frac{d}{c}\\ -1 & 0 & 0 & 0 & 0 & 0\\ 0 & -\frac{d\tau_{22}}{c} & 0 & -\frac{d}{c} & 0 & f+\frac{d^2}{c}\\ -2(b+c-\tau_{22}) & 0 & -\frac{e}{g} & 0 & -1 & 0\\ 0 & \frac{(c-\tau_{22})^2}{c}-a & 0 & \frac{\tau_{22}}{c}-1 & 0 & -\frac{d\tau_{22}}{c}\\ -\frac{e}{g} & 0 & -\frac{1}{g} & 0 & 0 & 0 \end{bmatrix}, \tag{A.6}$$

where the dimensionless parameters are defined by

$$\begin{aligned}&a=\bar{\mathcal{A}}^{(f)}_{01212}-\frac{\left(\bar{\Gamma}^{(f)}_{0211}\right)^2}{\bar{K}^{(f)}_{011}},\quad c=\bar{\mathcal{A}}^{(f)}_{02121}-\frac{\left(\bar{\Gamma}^{(f)}_{0211}\right)^2}{\bar{K}^{(f)}_{011}},\quad d=-\frac{\bar{\Gamma}^{(f)}_{0211}}{\bar{K}^{(f)}_{011}},\\ &e=\frac{\bar{\Gamma}^{(f)}_{0112}-\bar{\Gamma}^{(f)}_{0222}}{\bar{K}^{(f)}_{022}},\\ &b=\frac{1}{2}\left[\bar{\mathcal{A}}^{(f)}_{01111}-2\bar{\mathcal{A}}^{(f)}_{01122}-2\bar{\mathcal{A}}^{(f)}_{01221}+\bar{\mathcal{A}}^{(f)}_{02222}+\frac{2\left(\bar{\Gamma}^{(f)}_{0211}\right)^2}{\bar{K}^{(f)}_{011}}\right],\quad f=\frac{1}{\bar{K}^{(f)}_{011}},\\ &g=\frac{1}{\bar{K}^{(f)}_{022}},\end{aligned} \tag{A.7}$$

in which the dimensionless instantaneous electro-elastic moduli are given by

$$\bar{\mathcal{A}}^{(f)}_0=\frac{\mathcal{A}^{(f)}_0}{\mu_f},\qquad \bar{\Gamma}^{(f)}_0=\sqrt{\frac{\varepsilon}{\mu_f}}\Gamma^{(f)}_0,\qquad \bar{K}^{(f)}_0=\varepsilon K^{(f)}_0. \tag{A.8}$$

The characteristic equation $\det(\mathbf{N}-q\mathbf{I})=0$ gives

$$\begin{aligned}&cgq^6+[2bg+cf+d(d-2e)]\,q^4+\left[ag+2bf-2d(d-e)-e^2f/g\right]q^2\\ &\quad+d^2+af=0.\end{aligned} \tag{A.9}$$

For the Gent ideal dielectric model characterized by Eq. (A.4), the dimensionless parameters can be explicitly expressed as

$$\begin{aligned}&a=2\lambda_1^2\bar{W}_1-\lambda_1^2\lambda_3^2\bar{E}_L^2,\\ &b=\left(\lambda_1^2+\lambda_1^{-2}\lambda_3^{-2}\right)\bar{W}_1+2\left(\lambda_1^2-\lambda_1^{-2}\lambda_3^{-2}\right)^2\bar{W}_{11}+\frac{3}{2}\lambda_1^2\lambda_3^2\bar{E}_L^2,\\ &c=2\lambda_1^{-2}\lambda_3^{-2}\bar{W}_1,\qquad d=-\lambda_1\lambda_3\bar{E}_L,\qquad e=-2\lambda_1\lambda_3\bar{E}_L,\qquad f=g=1,\end{aligned} \tag{A.10}$$

where $\bar{W}_1$ and $\bar{W}_{11}$ are defined in Eq. (8)$_{2,3}$, and $\bar{E}_L=\lambda_1^{-2}\lambda_3^{-2}\bar{D}_{L2}$, with $\bar{D}_{L2}=D_{L2}/\sqrt{\mu_f\varepsilon}$. Due to $\tau_{22}=0$ for the soft dielectric film, Eq. (A.6) then reduces to the explicit Stroh submatrices given in Eq. (7).

Substituting Eq. (A.10) into Eq. (A.9) and canceling out the common factor yields

$$(q^2+1)\left\{q^4+\left[1+\lambda_1^4\lambda_3^2+\frac{2\bar{W}_{11}}{\bar{W}_1}\frac{(\lambda_1^4\lambda_3^2-1)^2}{\lambda_1^2\lambda_3^2}\right]q^2+\lambda_1^4\lambda_3^2\right\}=0, \tag{A.11}$$

where the factor $q^2+1=0$ yields $q=\pm\mathrm{i}$, while the remaining biquadratic factor gives the other two pairs of roots, recovering the expressions in Eq. (9). For the ideal dielectric model, the eigenvalues of the characteristic equation (A.11) are independent of the electric field $\bar{E}_L$. However, this does not imply that the bifurcation condition is independent of $\bar{E}_L$, since the Stroh matrix, its associated eigenvectors,

and the resulting impedance matrices all retain an explicit dependence on the electric field.

For the incompressible hyperelastic substrate, the dimensionless Stroh matrix is

$$\mathbf{N}_s = \begin{bmatrix} 0 & -1 & \frac{1}{c_s} & 0 \\ -1 & 0 & 0 & 0 \\ -2(b_s + c_s) & 0 & 0 & -1 \\ 0 & c_s - a_s & -1 & 0 \end{bmatrix}, \tag{A.12}$$

where the dimensionless parameters are defined as

$$a_s = \frac{\mathcal{A}^{(s)}_{01212}}{\mu_s}, \quad b_s = \frac{\mathcal{A}^{(s)}_{01111} - 2\mathcal{A}^{(s)}_{01122} - 2\mathcal{A}^{(s)}_{01221} + \mathcal{A}^{(s)}_{02222}}{2\mu_s}, \quad c_s = \frac{\mathcal{A}^{(s)}_{02121}}{\mu_s}. \tag{A.13}$$

in which

$$\mathcal{A}^{(s)}_{0pkqj} = F_{p\alpha} F_{q\beta} \frac{\partial^2 W_s}{\partial F_{k\alpha} \partial F_{j\beta}}. \tag{A.14}$$

Substituting the Gent hyperelastic model $(1)_1$ into Eq. (A.13) gives the dimensionless coefficients a_s, b_s, and c_s given in Eq. (18). The characteristic equation $\det(\mathbf{N}_s - q_s\mathbf{I}) = 0$ then recovers Eq. (17). The two roots q_{s1} and q_{s2} with positive imaginary parts are chosen so that $\exp(iq_s k x_2)$ decays as $x_2 \to +\infty$.

Data availability

Data will be made available on request.

References

[1] Pelrine RE, Kornbluh RD, Joseph JP. Electrostriction of polymer dielectrics with compliant electrodes as a means of actuation. Sens Actuators A 1998;64(1):77–85.

[2] Su YP, Shen XD, Zhao ZN, Wu B, Chen WQ. Electromechanical deformations and bifurcations in soft dielectrics: A review. Materials 2024;17(7):1499.

[3] Wu B, Kong LH, Chen WQ, Riccobelli D, Destrade M. Electro-mechanical wrinkling of soft dielectric films bonded to hyperelastic substrates. J Mech Phys Solids 2026;209:106490.

[4] Su YP, Wu B, Chen WQ, Destrade M. Finite bending and pattern evolution of the associated instability for a dielectric elastomer slab. Int J Solids Struct 2019;158:191–209.

[5] Li TF, Keplinger C, Baumgartner R, Bauer S, Yang W, Suo ZG. Giant voltage-induced deformation in dielectric elastomers near the verge of snap-through instability. J Mech Phys Solids 2013;61(2):611–28.

[6] Shian S, Bertoldi K, Clarke DR. Dielectric elastomer based "grippers" for soft robotics. Adv Mater 2015;27(43):6814–9.

[7] Chen YF, Zhao HC, Mao J, Chirarattananon P, Helbling EF, Hyun N-SP, Clarke DR, Wood RJ. Controlled flight of a microrobot powered by soft artificial muscles. Nature 2019;575(7782):324–9.

[8] Brochu P, Pei QB. Advances in dielectric elastomers for actuators and artificial muscles. Macromol Rapid Commun 2010;31(1):10–36.

[9] Liang W, Liu H, Wang KY, Qian ZH, Ren LQ, Ren L. Comparative study of robotic artificial actuators and biological muscle. Adv Mech Eng 2020;12(6):1–25.

[10] Shi XT, Zou J, Yan PN, Wan RT, Lu BY, Gu GY, Zhu XY. Semiseparated biphasic bicontinuous dielectric elastomer for high-performance artificial muscle. Science 2025;390(6777):1044–9.

[11] Liu XY, Sun HB, Liu ST, Jiang YJ, Yin ZM, Yu B, Ning NY, Tian M, Zhang LQ. Dielectric elastomer sensor with high dielectric constant and capacitive strain sensing properties by designing polar-nonpolar fluorosilicone multiblock copolymers and introducing poly(dopamine) modified CNTs. Compos B 2021;223:109103.

[12] Lee G, Zarei M, Wei QS, Yong, Lee SG. Surface wrinkling for flexible and stretchable sensors. Small 2022;18(42):2203491.

[13] Zhong H, Xue QQ, Li JM, He YF, Xie YX, Yang CH. Stretchable transparent polyelectrolyte elastomers for all-solid tunable lenses of excellent stability based on electro–mechano–optical coupling. Adv Mater Technol 2023;8(3):2200947.

[14] Liu L, Hao Q, Li ZH, Xiong JH, Zhang YK, Cheng Y. Design and demonstration of DEA-based tunable planar liquid crystal alvarez lenses. Opt Laser Technol 2025;182:112068.

[15] Li Q, Yao FZ, Liu Y, Zhang GZ, Wang H, Wang Q. High-temperature dielectric materials for electrical energy storage. Annu Rev Mater Res 2018;48(1):219–43.

[16] Wang Z, Tang C, Wang YX, Zhou L, Dong XG, Jiang SW, Pan YY, Liu XJ, Zhao HC. Enhancing the energy conversion efficiency of dielectric elastomer generators via elastic energy storage and recovery. Appl Energy 2025;379:124854.

[17] Chiba S, Waki M, Takeshita M, Ohyama K. Examination of factors to improve the performance of dielectric elastomer transducers and their applications. Smart Mater Struct 2024;33(6):065016.

[18] Nejati A, Mohammadi H. A multiphysics framework for energy conversion from nonlinear electrostrictive dielectric elastomer generators. Int J Solids Struct 2025;314:113345.

[19] Guo Y, Liu L, Liu Y, Leng J. Review of dielectric elastomer actuators and their applications in soft robots. Adv Intell Syst 2021;3(10):2000282.

[20] Feng WW, Sun L, Jin ZK, Chen LL, Liu YC, Xu H, Wang C. A large-strain and ultrahigh energy density dielectric elastomer for fast moving soft robot. Nat Commun 2024;15:4222.

[21] Zhao ZN, Chen YJ, Hu XY, Bao RH, Wu B, Chen WQ. Vibrations and waves in soft dielectric elastomer structures. Int J Mech Sci 2023;239:107885.

[22] Zhu FZ, Wu B, Destrade M, Wang HM, Bao RH, Chen WQ. Voltage-controlled non-axisymmetric vibrations of soft electro-active tubes with strain-stiffening effect. Int J Solids Struct 2024;290:112671.

[23] Si L, Kong LH, Chen WQ, Bao RH, Wu B. Voltage-controlled vibrations in bending-deformed soft electro-active slabs. Adv Eng Mater 2025;28:2500594.

[24] Yu X, Lu ZB, Cui FS, Cheng L, Cui YD. Tunable acoustic metamaterial with an array of resonators actuated by dielectric elastomer. Extrem Mech Lett 2017;12:37–40.

[25] Si L, Wang J, Jiang W, Bao RH, Wu B. Tunable antiplane waves in two-dimensional soft dielectric phononic crystals under inhomogeneous biasing fields. Acta Mech Solida Sin 2026.

[26] Chen YJ, Wu B, Su YP, Chen WQ. Effects of strain stiffening and electrostriction on tunable elastic waves in compressible dielectric elastomer laminates. Int J Mech Sci 2020;176:105572.

[27] Chen YJ, Wu B, Destrade M, Chen W. Voltage-controlled topological interface states for bending waves in soft dielectric phononic crystal plates. Int J Solids Struct 2022;259:112013.

[28] Li B, Cao YP, Feng XQ, Gao HJ. Mechanics of morphological instabilities and surface wrinkling in soft materials: A review. Soft Matter 2012;8(21):5728–45.

[29] Shian S, Kjeer P, Clarke DR. Electric-field induced surface instabilities of soft dielectrics and their effects on optical transmittance and scattering. J Appl Phys 2018;123(11):113105.

[30] Tan YL, Hu BR, Song J, Chu ZY, Wu WJ. Bioinspired multiscale wrinkling patterns on curved substrates: An overview. Nano-Micro Lett 2020;12(1):101.

[31] Nagashima S, Ota R, Okamoto R, Matsubara S, Okumura D. Elastocapillary folding in film-substrate bilayers. Int J Mech Sci 2026;315:111455.

[32] Liu RC, Liu Y, Goriely A. Surface wrinkling of a film coated to a graded substrate. J Mech Phys Solids 2024;186:105603.

[33] Lai A, Ou D, Liao J, Fu G. Buckling morphology evolution of thin films on non-linear elastic substrates. Acta Mech Sin 2025;41(2):424175.

[34] Mirandola A, Carotenuto AR, Cutolo A, Palumbo S, Fraldi M, Deseri L. Unveiling scaling laws for wrinkling in compressed fiber-reinforced bilayers at any elastic mismatch. J Mech Phys Solids 2026;212:106564.

[35] Liu ZW, Liu Y. A brief review on recent progress of surface instabilities in film-substrate systems. Acta Mech Solida Sin 2026;212:433–54.

[36] Li B, Cao YP, Feng XQ, Gao HJ. Surface wrinkling of mucosa induced by volumetric growth: Theory, simulation and experiment. J Mech Phys Solids 2011;59(4):758–74.

[37] Balbi V, Destrade M, Goriely A. Mechanics of human brain organoids. Phys Rev E 2020;101(2):022403.

[38] Riccobelli D, Bevilacqua G. Surface tension controls the onset of gyrification in brain organoids. J Mech Phys Solids 2020;134:103745.

[39] Zhao Y, Feng B, Lee J, Lu N, Pierce DM. A multi-layered computational model for wrinkling of human skin predicts aging effects. J Mech Behav Biomed Mater 2020;103:103552.

[40] Li ZW, Zhai Y, Wang Y, Wendland GM, Yin XB, Xiao JL. Harnessing surface wrinkling-cracking patterns for tunable optical transmittance. Adv Opt Mater 2017;5(19):1700425.

[41] Stafford CM, Harrison C, Beers KL, Karim A, Amis EJ, VanLandingham MR, Kim H-C, Volksen W, Miller RD, Simonyi EE. A buckling-based metrology for measuring the elastic moduli of polymeric thin films. Nat Mater 2004;3(8):545–50.

[42] Zhao XX, Wang JJ, Huang JK, Li LL, Liu EP, Zhao JX, Li QF, Zhang X, Lu CH. Path-guided hierarchical surface relief gratings on azo-films induced by polarized light illumination through surface-wrinkling phase mask. Langmuir 2020;36(11):2837–46.

[43] Lee J, Jung S, Kim W. Dependence of the effective surface tension of liquid phase eutectic gallium indium on wrinkles of the surface oxide. Extrem Mech Lett 2021;48:101386.

[44] Wang M, Mu L, Zhang H, Ma SQ, Liang YH, Ren L. Flexible strain sensor with ridge-like microstructures for wearable applications. Polym Adv Technol 2022;33(1):96–103.

[45] Genzer J, Groenewold J. Soft matter with hard skin: From skin wrinkles to templating and material characterization. Soft Matter 2006;2(4):310.

[46] Audoly B, Boudaoud A. Buckling of a stiff film bound to a compliant substrate-Part I. J Mech Phys Solids 2008;56(7):2401–21.
[47] Alawiye H, Kuhl E, Goriely A. Revisiting the wrinkling of elastic bilayers I: Linear analysis. Philos Trans R Soc A 2019;377:20180076.
[48] Martins A, Silvestre N, Bebiano R. A new modal theory for wrinkling analysis of stretched membranes. Int J Mech Sci 2020;175:105519.
[49] Qiu XH, Guo JM, Wang CG, Tan HF. Stretch-induced wrinkling and post-buckling bifurcation in rectangular films: Insights into energy barrier mechanisms. Int J Mech Sci 2025;299:110398.
[50] Qiu XH, Li HC, Tan HF, Wang CG, Liu YP. Wrinkling behavior of the solid-electrolyte interphase in Li-Ion batteries with silicon-graphite composite electrodes. Acta Mech Solida Sin 2025;38(3):492–9.
[51] Kwak H, Lee J, Kim J, Jo H, Ki K, Lee A. Wrinkling of thin films in pre-stretched soft substrate trilayers. Int J Mech Sci 2026;312:111213.
[52] van den Ende D, Kamminga J-D, Boersma A, Andritsch T, Steeneken PG. Voltage-controlled surface wrinkling of elastomeric coatings. Adv Mater 2013;25(25):3438–42.
[53] Lin I-T, Choi YS, Wojcik C, Wang TS, Kar-Narayan S, Smoukov SK. Electro-responsive surfaces with controllable wrinkling patterns for switchable light reflection-diffusion-grating devices. Mater Today 2020;41:51–61.
[54] Peng JB, Zhuo JS, Qiu HC, Normahmedov O, Shi M, Dong HF, Wang LT, Jiang SC, Zou J, Gu GY, Li TF, Fu WF, Peng BY, Ma HZ, Shi Y. Low-voltage and high-output dielectric elastomer actuators for untethered soft machines working at 200 volts. Sci Robot 2026;11(112):eady9635.
[55] Shield TW, Kim KS, Shield RT. The buckling of an elastic layer bonded to an elastic substrate in plane strain. J Appl Mech 1994;61:231–5.
[56] Cai ZX, Fu YB. On the imperfection sensitivity of a coated elastic half-space. Proc R Soc A 1999;455(1989):3285–309.
[57] Liu Y. Higher order solution to the Euler buckling threshold for compressible hyperelastic bilayers. Acta Mech Sin 2023;39(8):422379.
[58] Cai ZX, Fu YB. Exact and asymptotic stability analyses of a coated elastic half-space. Int J Solids Struct 2000;37(22):3101–19.
[59] Cao YP, Hutchinson JW. Wrinkling phenomena in Neo-Hookean film/sub-strate bilayers. J Appl Mech 2012;79(3):031019.
[60] Hutchinson JW. The role of nonlinear substrate elasticity in the wrinkling of thin films. Philos Trans R Soc A 2013;371(1993):20120422.
[61] Fu YB, Ciarletta P. Buckling of a coated elastic half-space when the coating and substrate have similar material properties. Proc R Soc A 2015;471(2178):20140979.
[62] Cheewaruangroj N, Biggins JS. Pattern selection when a layer buckles on a soft substrate. Soft Matter 2019;15(18):3751–70.
[63] Alawiye H, Farrell PE, Goriely A. Revisiting the wrinkling of elastic bilayers II: Post-bifurcation analysis. J Mech Phys Solids 2020;143:104053.
[64] Wang B, Xu C, Zhang BH, Bi HH, Cao SC, Huang YA. First-order and second-order wrinkling of thin elastic film laminated on a graded substrate. Int J Mech Sci 2023;243:108047.
[65] Su YP, Wu B, Chen WQ, Destrade M. Pattern evolution in bending dielectric-elastomeric bilayers. J Mech Phys Solids 2020;136:103670.
[66] Sriram S, Polukhov E, Keip M-A. Data-driven analysis of structural instabilities in electroactive polymer bilayers based on a variational saddle-point principle. Int J Solids Struct 2024;291:112663.
[67] Suo ZG. Theory of dielectric elastomers. Acta Mech Solida Sin 2010;23(6):549–78.
[68] Su YP, Broderick HC, Chen WQ, Destrade M. Wrinkles in soft dielectric plates. J Mech Phys Solids 2018;119:298–318.
[69] Dorfmann L, Ogden RW. Instabilities of soft dielectrics. Philos Trans R Soc A 2019;377(2144).
[70] Gangwar AS, Khurana A, Sharma AK. Wrinkling stability in soft dielectric elastomers: The role of strain stiffening and stretch-dependent permittivity. Int J Solids Struct 2025;318:113429.
[71] Dorfmann L, Ogden RW. Nonlinear theory of electroelastic and magnetoelastic interactions. New York: Springer; 2014.
[72] Lu H, Dai ZH. Deep indentation of soft thin films beyond the 10% rule. Phys Rev Lett 2026;137(3):036201.
[73] Verma P, Chaudhury H. Small deformation superposed on large deformation of an elastic dielectric. Internat J Engrg Sci 1966;4(3):235–47.
[74] Destrade M, Gilchrist MD, Prikazchikov DA, Saccomandi G. Surface instability of sheared soft tissues. J Biomech Eng 2008;130:061007.
[75] Destrade M. Incremental equations for soft fibrous materials. In: Nonlinear mechanics of soft fibrous materials. Wien: Springer; 2015, p. 233–67.
[76] Liu J, Bertoldi K. Bloch wave approach for the analysis of sequential bifurcations in bilayer structures. Proc R Soc A 2015;471(2182):20150493.
[77] Chandler TG, Vella D. Validity of Winkler's mattress model for thin elastomeric layers: Beyond Poisson's ratio. Proc Math Phys Eng Sci 2020;476(2242):20200551.
[78] Zhang GZ, Dai ZH. Asymptotic models for thin transversely isotropic elastic layers. Appl Math Mech 2026;47(7):1603–24.
[79] Wriggers P. Nonlinear finite element methods. Springer Science & Business Media; 2008.
[80] De Borst R, Crisfield MA, Remmers JJ, Verhoosel CV. Nonlinear finite element analysis of solids and structures. John Wiley & Sons; 2012.